Cyclic behavior of RC frame members strengthened with secured CFRP sheets: comprehensive modeling strategies

by

Sama Mohammed Saleem

B.S., University of Sharjah, 2015

A THESIS

submitted in partial fulfillment of the requirements for the degree

MASTER OF SCIENCE

Department of Civil Engineering
Carl. R. Ice College of Engineering

KANSAS STATE UNIVERSITY
Manhattan, Kansas

2023

Approved by:
Major Professor
Dr. Hayder A.Rasheed

Copyright

ABSTRACT

Structural beam-column joints are critical elements in ensuring the resilience of framed structures against seismic forces. In recent years, the implementation of Fiber Reinforced Polymer (FRP) composites as strengthening materials has gained significant attention due to their remarkable mechanical properties and corrosion resistance. Further research is required to understand the behavior of frame members and joints undergoing cyclic loading when strengthened with FRP as such strengthening promotes different structural behavior of the assembly and is dominated by different failure modes.

This study presents a thorough review of existing literature on the strengthening of structural beam-column joints using FRP sheets, followed by a description of a comprehensive experimental investigation and an attempt to model the cyclic lateral behavior and response of CFRP strengthened frame members aiming at enhancing our understanding of this innovative strengthening technique under seismic loading conditions. Unlike earlier studies that focused on strengthening the joint itself, this study focuses on joints reinforced in a ductile manner according to modern design codes while needing the members framing into it to be upgraded with external FRP. For this purpose, experimental data from four frame assemblies, the members of each are strengthened with FRP sheets and anchored in different configurations is used. A comparative modeling is then conducted with comparisons between the experimental data and the results predicted by the proposed model to establish the validity of the present approach.

The outcomes contribute significantly to the ongoing advancements in the design and application of FRP-strengthened frame members, thereby fostering their wider implementation within the field of structural engineering.

ACKNOWLEDGEMENT

First and foremost, praises and thanks to God and His blessings throughout my research journey and for the completion of this work.

I would like to express the deepest appreciation to my committee chair and academic supervisor, Dr. Hayder A. Rasheed, who has consistently conveyed a spirit of adventure in the field of research, academic assistantships, and an overall excitement in regard to teaching. Without his guidance and persistent help, this dissertation would not have been possible.

I would like to thank my committee members, Dr. David Rosowsky and Dr. Krishna Ghimire, whose guidance, feedback and constructive criticism have greatly refined this work.

My utmost appreciation goes to my beloved family who have always showed nothing but the strongest support with every step I have taken in life including my pursue of this master's degree. Your love, prayers, and the seemingly unwavering faith in me have helped immensely during challenging times.

I would also like to express my deepest thanks to my friends and colleagues who have showed constant support, provided valuable feedback, and worked side by side with me to help me overcome challenging dilemmas. I feel fortunate to have been surrounded by people like you.

Thank you all for being a part of my journey. To you, I dedicate this work.

Table of Contents

List of Figures

List of Tables

Nomenclature

A_f	Area of FRP
As	Area of tension steel.
As'	Area of compression steel.
b	width of a cross-section.
Ci	location of the neutral axis at the inflection strains level.
Cy	location of the neutral axis at yielding.
d	location of the tension steel with respect to the extreme compression fiber.
d'	location of the compression steel with respect to the extreme compression fiber.
E_c	Initial concrete modulus (Young's modulus).
Es	Steel modulus of elasticity.
Ef	FRP modulus of elasticity.
f'c	concrete compressive strength.
h	height of the cross-section.
I_g	gross moment of inertia of gross concrete section about centroidal axis.
Lc	the length of the vertical member.
Lg	distance from support to location of external cracking moment.
La	shear span distance from support to point of loading.
LaB	span length of beam.
L_B	distance from the support to the midspan of the beam.
L_{gB}	distance from the support to the pre-cracking region in the beam.
Ly	distance from the column tip to the post yielding region.
M	moment due to applied load.
M_{cr}	minimum moment at which the cracking takes place at a cross-section.
M_y	minimum moment at which the yielding takes place at a cross-section.

M_n moment corresponding to ultimate moment of section.

M_{res} moment at the residual point in the moment-curvature response.

P applied load at envelope.

P_i applied load at inflection point.

r compression stress-strain degradation factor that corresponds to a tensile inflection stress-strain.

Slope 1 slope of the line from zero to cracking moment in the trilinear approach.

Slope 2 slope of the line from cracking to yielding moment in the trilinear approach.

Slope 2e slope of the envelope line from cracking to yielding moment in the trilinear approach.

Slope 2i slope of the inflection line from cracking to yielding moment-curvature.

Slope res slope of the residual line from inflection to residual curvature and zero moment.

$t_{B/C\,1}$ deviation of B at the beam support with respect to a tangent line at midspan point C in the pre-cracking region.

$t_{B/C\,2}$ deviation of B at the beam support with respect to a tangent line at midspan point C in the post cracking region.

Xe normalized envelope strain to the strain corresponding to either the tensile or compressive strength of concrete.

Ye normalized envelope stress to the stress corresponding to either the tensile or compressive strength of concrete.

$\bar{y}_c$ location of the neutral axis prior to cracking.

δ_1 deflection contribution in the pre-cracking region.

δ_2 deflection contribution in the post cracking region.

δ_3	deflection contribution in the post yielding region.
ϕ_{un}	curvature corresponding to the pre-cracking region.
ϕ_{cr}	curvature corresponding to cracking moment of section.
ϕ_y	curvature corresponding to yielding moment of section.
ϕ_n	curvature corresponding to ultimate moment of section.
ϕ_e	curvature corresponding to envelope moment.
ϕ_i	curvature corresponding to inflection moment.
ϕ_{cri}	curvature corresponding to inflection cracking moment.
ϕ_{yi}	curvature corresponding to inflection yielding moment.
ϕ_{p-c}	curvature corresponding to post cracking moment of section.
ϕ_{p-y}	curvature corresponding to post yielding moment of section.
ϕ_{res}	curvature corresponding to the residual moment.
Δ_{fixed}	the deflection of the vertical member at the tip without the contribution of. The horizontal member.
Δ_{tip}	the deflection of the vertical member at the tip with the contribution of the horizontal member.
$\varepsilon_{cf\ cr}$	extreme compression fiber strain at the cracking stress.
$\varepsilon_{cf\ e}$	extreme compression fiber strain at any point on the envelope curve.
ε_{ci}	strain at the compressive inflection point on the stress-strain diagram.
$\varepsilon_{c\ res}$	residual compressive strain on the stress-strain diagram.
$\varepsilon_{cf\ y}$	extreme compression fiber strain at the yielding stress.
ε_{ec}	envelope compression strain.
ε_{te}	envelope tension strain.

ε_{ti}	strain at the tensile inflection point on the stress-strain diagram.
$\varepsilon_{t\,res}$	residual tensile strain on the stress-strain diagram.
ε_y	extreme compression fiber strain at the yielding stress.
ε'_c	strain corresponding to concrete compressive strength.
σ_i	the stress corresponding to the strain at the inflection point.
$\Delta\varepsilon_{e-i}$	the change in strain from the envelope curve to inflection point.
$\Delta\sigma_{e-i}$	the change in stress from the envelope curve to inflection point.
$\delta\Delta_{e-i}$	the change in column deflection from the envelope to the inflection level.
$\delta\Delta_{i-res}$	the change in column deflection from the inflection level to the residual level.
$\delta\Delta_{e-i\,1}$	the change in column deflection from the envelop level to the inflection level in the pre-cracking region.
$\delta\Delta_{e-i\,2}$	the change in column deflection from the envelop level to the inflection level in the post cracking region.
$\delta\Delta_{tip\,(e-i)}$	the net change in deflection from the envelope to the inflection level with the beam deflection contribution.
$\delta\Delta_{tip\,(i-res)}$	the net change in deflection from the inflection to the residual level with the beam deflection contribution.
$\delta\theta_{e-i}$	the change in beam rotation from the envelope curve to inflection point.
$\delta\theta_{i-res}$	the change in beam rotation from the inflection curve to residual point.
$\delta\theta_{B1}$	the change in beam rotation in the pre-cracking region.
$\delta\theta_{B2}$	the change in beam rotation in the post cracking region.

CHAPTER 1: INTRODUCTION

1.1 Overview/Background:

The need to incorporate or retrofit beam-column joints in seismicity-prone areas using different materials and techniques is becoming increasingly common due to the deficient behavior of frame assemblies under seismic loading and the increasing seismic demand. Concrete/Steel jacketing, epoxy repairs, and addition of shear walls are all effective and popular solutions, but the incorporation of FRP external reinforcement as a structural technique is garnering more attention in the last two decades due to their exceptional mechanical properties, light weight, and corrosion resistance (Pohoryles et al. 2019).

There are multiple ways and techniques used to incorporate FRP sheets in RC structural members. Bonding, wrapping and mechanically anchoring FRP sheets are all rapid processes that can be performed without hindering or increasing construction downtime Bousselham (2010). A common failure mode of beam-column joints under seismic loading is failure by shear in the joint. A number of researchers performed several experimental studies on the shear strengthening of beam-column joints using various sheet-bonding or sheet-wrapping schemes. These studies reflected the significant advantage of using FRP jackets to not only increase the shear capacity of the frame joint but to shift the failure mode to flexural hinging of the beam, that is a ductile mode of failure. However, very limited studies have addressed the need to upgrade the beams that frame into ductile joints designed per modern design codes, or upgraded with FRP, when earthquake demand levels become higher and address the shift of failure mode to the beam.

As with exploration of any innovative material, there are issues that arise requiring further research and solutions. One of the well-known drawbacks of external bonding of FRP is the premature debonding failure mode. Based on experimental studies, this can be greatly improved by using FRP wrapping of members. This strengthening technique has been observed to transfer the typical debonding failure in the member to concrete crushing of the beam or FRP rupture of the flexural sheet. It has since been recommended to extend the strengthening of the well-detailed joint with FRP, if needed, and to include the beam to develop the full-strength capacity of the joint assembly and impede premature and non-ductile failures under critical loads. When FRP wrapping is not accessible, carbon fiber splay anchorage is a great alternative to FRP wrapping.

Another drawback to the use of FRP composites is its low fire performance. Recent experimental investigations suggest the use of intumescent coatings to increase the fire resistance performance Ji et al (2013). Other studies suggested using other composite materials, like textile-reinforced mortar as it offers better bond to the concrete substrate alongside the thermal and fire resistance improvement Al-Salloum et al (2011). For simplicity and to focus on structural performance this research is focused on epoxy bonded FRP sheets external reinforcement as structural solutions.

The degree of performance improvement of joint assemblies under cyclic loading using FRP sheets can also be related to the orientation at which the sheets are applied to the joints or in wrapping the members. Some researchers concluded that applying FRP sheets with an orientation of 45 degrees to the principal axes can further improve the strength of the frame assembly. The reason for this improvement is justified by the ability of the sheet to bridge the shear cracks regardless of their direction. This also enhances the shear and torsional resistance to match different anticipated stresses and loading conditions (Parvin et al 2008).

Understanding the cyclic behavior of beam-column joints contributes to the development of effective design methodologies, retrofitting strategies, and seismic-resistant solutions for framed structures. Moreover, insights gained from studying the response of these assemblies under cyclic loading conditions facilitate the formulation of accurate analytical models and the refinement of design codes, thereby enhancing the overall robustness and performance of structural systems in the face of dynamic challenges.

2-1 Objectives:

The objectives of this research are to:

- Understand the changes in frame-joints assembly behavior when strengthened with different anchorage systems of FRP sheet configuration and the corresponding failure modes that control these configurations.
- Verify and validate the predicted data obtained from the proposed models against experimental data of real-life scale beam-column joint assemblies, strengthened with FRP sheets having different anchorage schemes that are undergoing a simulated reversed cyclic load.

2-2 Scope:

This thesis is structured around the compilation of six chapters outlining the cyclic behavior of one control frame joint specimen and four others strengthened using identical FRP configuration with various anchorage methods. These specimens undergo displacement-controlled cyclic loading. The study then advances to introduce a novel model for predicting the behavior of FRP frame members during reversed lateral cyclic loading. The first chapter provided a concise overview, objectives, and scope of the thesis. Subsequently, chapter two presents a comprehensive literature review within the scope of this thesis. Chapter three includes an accepted journal paper that introduces a phenomenological model developed through an experimental study of real-size frame joint specimens, which is then shown to predict the hysteretic behavior of the frame assembly very well. Chapter four explores a phenomenological stress-strain cyclic concrete model in compression and tension, which contributes to the foundational assumptions used in the novel analytical model predicting the moment-curvature response and load-deflection behavior of CFRP-strengthened frame members presented in chapter five. Chapter six summarizes the conclusions drawn from this comprehensive modeling study extracting relevant recommendations for future research work.

CHAPTER 2: LITERATURE REVIEW

2-1 Overview:

It is typically pre-assumed that a beam-column joint remains elastic while undergoing a seismic load. However, experimental testing showed that joints with minimal to moderate reinforcement resisting high shear load experience significant strength and stiffness loss that it undergoes an inelastic action. This means that joint failure could ultimately lead to structural failure and thus, it is crucial to understand this inelastic joint response and the means to properly reinforce frame joints. Several studies and tests have been performed to model this inelastic behavior with different strengthening configurations.

2-2 FRP Strengthening of Deficient RC Joints:

Few studies have been done for the joint behavior of RC beam-column frames. Lowes and Altoontash (2003) proposed a model that simulates the inelastic behavior of the beam-column joint under reversed cyclic load. The model is based on two primary failure modes: the joint core failure under shear loading, as well as the failure of the frame longitudinal reinforcement embedded in the joint. The proposed model simplifies the frame as two-dimensional four-node line elements with 3 degrees of freedom per node. The joint is identified as the shear panel, the vertical translation of the nodes is identified as the bar-slip springs, and the horizontal translation is identified as the interface-shear springs. Force equilibrium and static condensation of the global tangent matrix is used to find the residual and tangent deformation vectors. Comparisons between simulated and observed responses of several beam-column joint building sub-assemblages indicate that the model accurately represents the key characteristics of the inelastic joint response under moderate shear demands (Lowes and Altoontash 2003).

Mukherjee and Joshi (2004) also reported their findings on the behavior of FRP reinforced concrete beam-column joints under cyclic loading. The joints were fabricated with varying levels of steel reinforcement at the beam-column interface, including adequate and deficient steel bonding. Different configurations of FRP sheets and strips were applied to the joints. The columns typically were subjected to axial forces, while the beams underwent cyclic loading with controlled displacement. The loading protocol was applied using a dynamic actuator that incrementally increased the displacement amplitude. It was observed that FRP retrofitting, though is an effective choice for enhancing the seismic performance and for rehabilitating reinforced concrete joints, is also dependent on the application scheme of the FRP sheet and the anchorage (Mukherjee et al 2004).

Al-Salloum and Almusallam (2007) investigated the efficiency of FRP sheets retrofitted to non-seismic compliant beam-column joints as a means to test the efficiency of strengthening them enough to comply with existing seismic codes. For that purpose, four specimens were constructed with seismically inadequate joint shear strength by eliminating the transverse shear reinforcement. The test included two control specimens and two others that were strengthened using CFRP sheets in different schemes. All four specimens underwent cyclic lateral load tests simulating severe earthquake conditions. The control specimens that sustained damage were repaired by filling cracks with epoxy and externally bonding them with CFRP sheets following the same adapted schemes to subject them to cyclic lateral load tests as well. It was clearly observed that the strengthening and repair solutions delayed shear failure significantly. Failure was mainly due to CFRP debonding and/or concrete crushing at the beam. It was also evident that the extent at which the CFRP sheet is applied, the mechanical anchorage, and the epoxy bond controls the strength capacity of the frame joint mainly due to their ability to contain developed cracks and limit their propagation. Their tests clearly reflected the importance of the FRP solution in upgrading frame joints to adapt to seismic codes while highlighting the ability of the external reinforcement schemes to shift the failure mode from the joint to adjacent beam members (Al-Salloum and Almusallam 2007).

Lee et al (2009) developed a method to predict the ductile capacity of RC frame joints failing in shear post the development of plastic hinges at beam ends. It takes into consideration the propagation of the joints interface cracks as the residual strain of the longitudinal reinforcement post the development of the plastic region continues to increase with every inelastic load cycle. These cracks directly promote the deterioration of the joint shear strength and bond strength. The method proposed simulates the effect of the axial strain present in the plastic hinge region and the deformability associated with it and has been tested and compared to show good agreement with experimental results of five specimens (Lee et al 2009).

Realfonzo et al (2014) investigated the reinforcement of beam-column joints using FRP. Eight specimens were used for the laboratory experiment, six of which were FRP reinforced and two were used as control specimens. The objective of this test is to examine the efficiency of FRP reinforcement for a frame joint undergoing reversed cyclic load as well as testing the efficiency of repairing damaged specimens and confirming the efficiency of the strengthening solution. As commonly practiced, tests performed applied a constant axial load on the column while the beam underwent a displacement-controlled cyclic load. Their tests concluded that mechanical anchorage of the FRP is critical to avert sheet delamination and to achieve the full-strength capacity. It was also evident that with proper joint sheet anchorage, the failure mode can shift to the beam. They also concluded that retrofitting FRP sheets to damaged members allowed for the restoration of the strength capacity and ductility up to the level of the original strength of the members (Realfonzo et al 2014)

Elsisi et al (2021) numerically analyzed three models of frame joints that are reinforced with longitudinal steel bars, steel stirrups, CFRP longitudinal bars, and GFRP longitudinal bars respectively, by FEM using ANSYS software. The analysis clearly reflected an elastic performance for the joints reinforced by the GFRP and CFRP bars when used as longitudinal reinforcement, while it showed inelasticity for the conventional steel reinforcement up to failure. All three models failed by concrete shear at the beam-column interface highlighting, once again, shear as the principal failure mode for a beam-column joint undergoing seismic load (Elsisi et al 2021).

2-3 FRP Strengthening of Frame Members with Adequately Designed and Detailed Joints:

The formerly mentioned studies performed on beam-column joints collectively emphasize the importance of understanding the inelastic joint behavior prior to failure under cyclic loads and the effectiveness of different FRP reinforcement schemes. This section summarizes studies performed on joints reinforced per modern seismic codes to evaluate and model the inelastic hysteretic behavior of frame members reinforced with different FRP schemes while undergoing reversed cyclic load.

Saqan et al (2020) conducted an experimental study on FRP-strengthened frame assembly undergoing a simulated displacement-controlled reversed cyclic loading using an identical FRP strengthened member scheme anchored with different FRP schemes to study the performance of strengthened frame members, when the joint is adequate. The experiment was performed on four large-scale frame assemblies strengthened with FRP wraps, two different configurations of fiber splay anchors, and a combination of wraps and fiber splay anchors respectively. The experiment highlighted the effectiveness of these anchorage schemes employing a dense splay anchor only or a combination of full wraps with fiber splay anchors to not only provide the best overall performance but to best confine the plastic hinge region therefore suggesting dense fiber splay anchors as a great alternative to FRP wraps. This study will be based on that experimental investigation to further explore and model the cyclic behavior of frame assemblages with different anchorage schemes. Figure 2.1 and Figure 2.2 highlight the column critical section where failure first occurs in the strengthened frame assembly (Saqan et al. 2020)

Figure 2.1. The Experimental Failure of The One of The Four Specimens Occurring at The Column Critical Region (Saqan et al. 2020).

Figure 2.2. A Closer View on The Column Critical Section Where Failure of The Four Specimens Occurred (Saqan et al. 2020).

CHAPTER 3: MODELING CYCLIC RESPONSE OF CFRP STRENGTHENED FIBER ANCHORED RC FRAME MEMBERS TO FAILURE

Synopsis: There is a shortage of studies related to the effects of fiber anchorage on the behavior of strengthened frame members undergoing seismicity. This study models experimental data of four frame specimens having seismic code-compliant joints with different CFRP-strengthened members secured with fiber anchorage systems. Analytical formulation using a trilinear moment-curvature response is extended to accurately model the envelope curves of the vertical frame member by including the nonlinear interaction from the horizontal member, which presents a new solution. Furthermore, the experimental hysteresis data provides a basis to formulate an analytical model based on phenomenological observations to capture the cyclic load-drift curves. When modelling the drift-based hysteresis loops, each cycle is divided into three linear regions in the unloading and reloading paths, respectively. These are named push-bound, inflection range, and pull-bound regions. Curves correlating the ratio of unloading and reloading slopes of these regions to the initial backbone curve slope as a function of the drift ratio to yielding drift ratio are generated. These curves define the rules that the hysteresis loops behave according to. The hysteresis rules are calibrated against two different RC frame assemblies and used to predict the cyclic response of two other frame assemblies with similar features.

Keywords: Seismic strengthening; CFRP fiber anchors; Frame members; Hysteresis modeling; Backbone curve.

3-1 Introduction:

Strengthening frame members with CFRP composites is a subject of interest for seismic structural upgrade. Although the use of CFRP wrapping has been shown to improve the seismic performance of RC columns significantly, there is still a need for a better understanding of the behavior of FRP strengthened members, particularly under cyclic loads. Therefore, several models have been developed to capture the behavior of RC column-beam connections under cyclic load. On the other hand, new fiber anchoring techniques need to be investigated to come up with optimized anchoring methods for RC members under cyclic load to extend their response characteristics. The literature has limited number of studies addressing this aspect of member strengthening. A brief summary of the current literature related to modeling of FRP-strengthening behavior under cyclic loading is presented below.

A study was carried out by Dowell et al. (1998) to develop a model called "Pivot Hysteresis Model" to predict the nonlinear cyclic response of circular RC columns. This model was developed based on observing experimental data from previous research. It was noted that the unloading goes back to zero from any displacement level and reaches a single point in the force-displacement graph named the primary pivot point. Additionally, it was observed that there is a second point in the force-displacement graph called the pinching pivot point, where all force-displacement curves generally intersect. According to this study, two parameters were defined, $\boldsymbol{\alpha}$ and β, which relate to the primary pivot point and pinching pivot point to control the unloading stiffness and pinching behavior, respectively.

Another model was developed by Sharma et al. (2013) to improve Dowell's model and make it applicable to any RC frame member. An improvement of the $\boldsymbol{\alpha}$ and β parameters was devised to make the model capable of capturing the complete range of the axial load on column (applied axial compression load/axial load capacity of the column) and to account for the effect of transverse reinforcement on the pinching behavior. The parameters $\boldsymbol{\alpha}$ and β are controlled by axial load ratio and longitudinal and transverse reinforcement indices. In addition, new parameters were introduced to account for the effect of non-seismic detailed exterior joints. According to this study, the proposed model could sufficiently capture the hysteresis behavior of RC frame members.

Zhang et al. (2018) developed an analytical model based on analyzing the hysteretic behavior of concrete in tension under a cyclic load. The model was derived on the basis of the opening and closure of the cracks and their corresponding stiffness under cyclic unloading and reloading. The Dimensionless expressions for x and y based on deformation and stress were introduced and incorporated into the model along with their synonymous values defining the beginning of the inelastic range. The y parameter is the dimensionless stress normalized by the concrete tensile strength (f_t); x is the dimensionless deformation normalized by the strain (ε_t) or displacement (δ_t) corresponding to the concrete tensile strength.

Wang et al. (2019) conducted an experimental study to investigate the seismic behavior of eight steel reinforced concrete (SRC) frame columns under low cyclic repeated loading. The study found that, the SRC column specimen undergoes three distinct stages during the cyclic load failure process including the elastic stage, the inelastic with cracks stage, and the failure stage. Similar behaviors to reinforced concrete frame columns were noticed during the elastic stage. During the inelastic stage, the load-bearing capacity improved due to the interaction between steel and concrete. Additionally, the seismic performance of the frames was enhanced by increasing the steel ratio and axial load ratio. Moreover, before peak load, ratio of stirrups has a slight impact on the seismic behavior of the frame. However, this effect becomes more noticeable after the peak load such that the increase of stirrup ratio enhances the energy dissipation capacity and member ductility.

Wang et al. (2022) aimed to investigate the seismic performance of circular high-strength concrete (HSC) columns confined with carbon fiber-reinforced polymer (CFRP) composites. Several conclusions were drawn from this study. Externally bonded CFRP wraps applied in the potential plastic hinge regions can effectively and significantly improve the seismic performance of circular HSC columns, especially for columns with relatively higher concrete strength. The ultimate lateral load and corresponding displacement increased with an increase of the axial compression ratio. Likewise, the seismic performance of the HSC columns improved when the height of the confined area at the plastic hinge region was larger than 1.1 times the cross-section diameter of the column. Finally, axial compression ratio, concrete strength, and height of CFRP-confined area at plastic hinge region had limited influence on the degradation of effective unloading stiffness and the equivalent viscous damping ratio of CFRP-confined HSC columns.

Ling et al. (2022) proposed a further pivot hysteretic model to predict the seismic behavior of existing RC structures. The treatment was based on a previous pivot hysteresis model and attempts to make it applicable to structures with different failure modes, such as flexural and shear failure, directly impacting the hysteresis response. The pivot model was improved by optimizing energy dissipation from 113 column samples under cyclic loading and reformulating the equations for α and β parameters. According to the authors, the new formulations can capture the influences of the axial load ratio (ALR), transverse reinforcement index, and longitudinal reinforcement index. It was assumed that the ALR should not exceed 0.55.

This study takes experimental load-deflection data of four frame specimens subject to cyclic loading with CFRP strengthened plastic-hinge region anchored with different fiber arrangements having frame joints that comply with current seismic code requirements. The data provide experimental hysteresis loop results that are used in this paper to formulate two models namely an analytical backbone curve model based on trilinear moment-curvature response and a phenomenological hysteresis loop model based on experimental observations and assumptions that allow capturing the cyclic load-drift ratio curves experienced experimentally to a high degree of accuracy. The phenomenological model was based on careful observations of the experimental results leading to identifying 3 distinct zones of the hysteresis cycles. The decay in unloading-reloading-inflection zone stiffness values as ratios of the initial stiffness is modeled against the drift ratio at hand as a percentage of the drift ratio at the yielding point. The boundaries of the three zones were identified based on experimental observations as well. This treatment resulted in a simplified yet unique cyclic response model for reinforced concrete frame members strengthened with CFRP that was applied blindly to other specimens with similar strengthening features reflecting good correspondence.

3-2 Experimental Study:

The present model is based on the experimental study by (Saqan et al. 2020). The main objective of this study was to investigate the effectiveness of using carbon fiber reinforced polymer (CFRP) fabric anchored using CFRP fiber anchors and CFRP wrapping for strengthening reinforced concrete (RC) frame assemblies subjected to cyclic loading. The experimental study was conducted on four RC frames identical in size, internal reinforcement and external CFRP member strengthening, Figure 3.1. Specimen BCA-2 was confined with full wrap of the plastic hinge region of the vertical member as well as inverted U-wraps confining the horizontal members joint junction, Figure 3.2. Specimen BCA-3 had a single inclined fiber anchor into the joint plus a single anchor on each face of the vertical and horizontal members in the plastic hinge region, Figure 3.3. Specimen BCA-4 had 5 fiber anchors securing the entire plastic hinge region on both sides of the vertical member, in addition to 4 fiber anchors on the top surface of the horizontal members next to the joint, Figure 3.4. Specimen BCA-5 was anchored with two direct tension fiber anchors into the vertical and horizontal members on each side next to the joint plus full wrapping of the plastic hinge region of the vertical member and inverted U-wrapping of the top surface of the horizontal members, Figure 3.5.The experimental program involved subjecting the frames to cyclic loading tests that simulated seismic loading as shown in the displacement protocol in Figure 3.6. The performance of the frames was evaluated based on various parameters such as the lateral load-displacement response, stiffness degradation, energy dissipation capacity, and damping. The frame BCA-2 showed a ductile response and a minor decrease in strength after the peak load. Specimen BCA-3 reflected close behavior to BCA-2 but had a lower ultimate capacity. Specimen BCA-4 showed an improvement in comparison to frames BCA-2 and BCA-3 since it had a denser arrangement of fiber anchors securing the entire plastic hinge region. Additionally, this specimen survived the maximum drift ratio of 3% with a slight decrease in strength. Specimen BCA-5, with the hybrid confining technique, indicated very similar behavior to specimen BCA-4 but exhibited a decline of strength at a more rapid pace. According to the experimental results, specimen BCA-5 indicated the highest ultimate capacity. In contrast, specimen BCA-3 showed the lowest ultimate capacity among strengthened specimens due to the limited anchorage application. Accordingly, specimens BCA-2 and BCA-4 were calibrated separately by the present model. Then, the parameters of specimen BCA-2 were used to predict the hysteresis response of frame BCA-3. Similarly, the parameters of specimen BCA-4 were used to predict the behavior of BCA-5. Table 3-1 and Table 3-2 present the concrete strength and mechanical properties of the CFRP fibers and laminates, respectively. Table 3-3 depicts the summary of the experimental load-deformation results at the cracking, yielding and ultimate stages.

Table 3-1. Concrete Strength Data for All Specimens Used in the Modeling Task.

Specimen	28-day concrete strength MPa (ksi)	Day of testing concrete strength MPa (ksi)	Age on the day of testing (Days)
BCA-1	30.5 (4.42)	32.0 (4.64)	228
BCA-2	30.4 (4.41)	31.9 (4.63)	242
BCA-3	34.2 (4.96)	35.1 (5.09)	245
BCA-4	36.4 (5.28)	34.5 (5.00)	583
BCA-5	32.6 (4.73)	29.2 (4.24)	501

Table 3-2. Mechanical Properties of The CFRP Fibers and Laminates Used in the Experimental Study.

Fiber Type	Nominal Thickness t mm (in.)	Ultimate tensile strength f_{fu} MPa (ksi)	Elongation at break ε_{fu} (%)	Modulus of elasticity E GPa (ksi)
V-Wrap™ C200H - Dry	0.33 (0.013)	4830 (700)	2.1	227.5 (33,000)
V-Wrap™ C200H – Cured Laminate	1.02 (0.040)	1240 (180)	1.7	73.77 (10,700)

Table 3-3—Comparison of Cracking Load, Yielding Load, and Ultimate Load for All Specimens (Saqan et al. 2020).

Specimen	Cracking load, KN (kips)	Drift ratio, %	Yielding load, KN (kips)	Drift ratio, %	Average ultimate load, KN (kips)	Drift ratio, %	Increase in strength, %
BCA-2	18.5 (4.16)	0.25	37.9 (8.52)	0.65	48.8 (10.97)	1.50	19.3
BCA-3	17.8 (4.00)	0.06	37.4 (8.41)	0.65	46.5 (10.45)	1.35 to 1.50	13.7
BCA-4	23.0 (5.17)	0.10	47.5 (10.68)	0.85	53.93 (12.12)	1.46 to 1.50	31.9
BCA-5	20.0 (4.50)	0.13	47.79 (10.77)	0.93	58.75 (13.20)	1.45 to 1.49	43.60

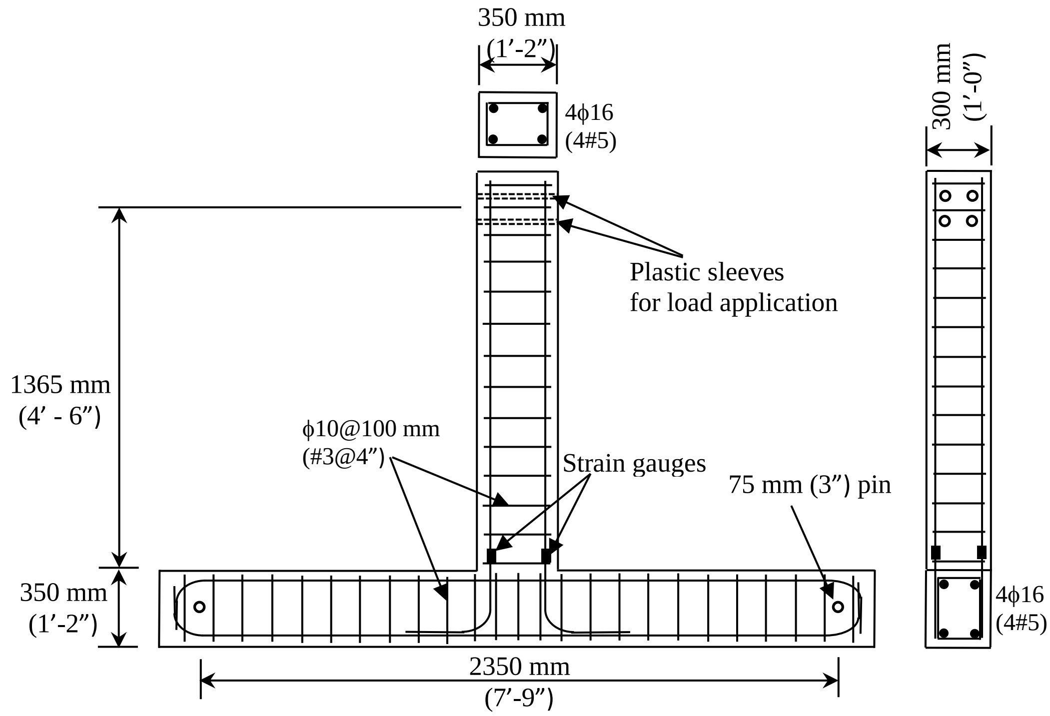

Figure 3.1.Overall Dimensions, Reinforcement Details, and Internal Strain Gauge Locations for All Specimens (Saqan et al. 2020).

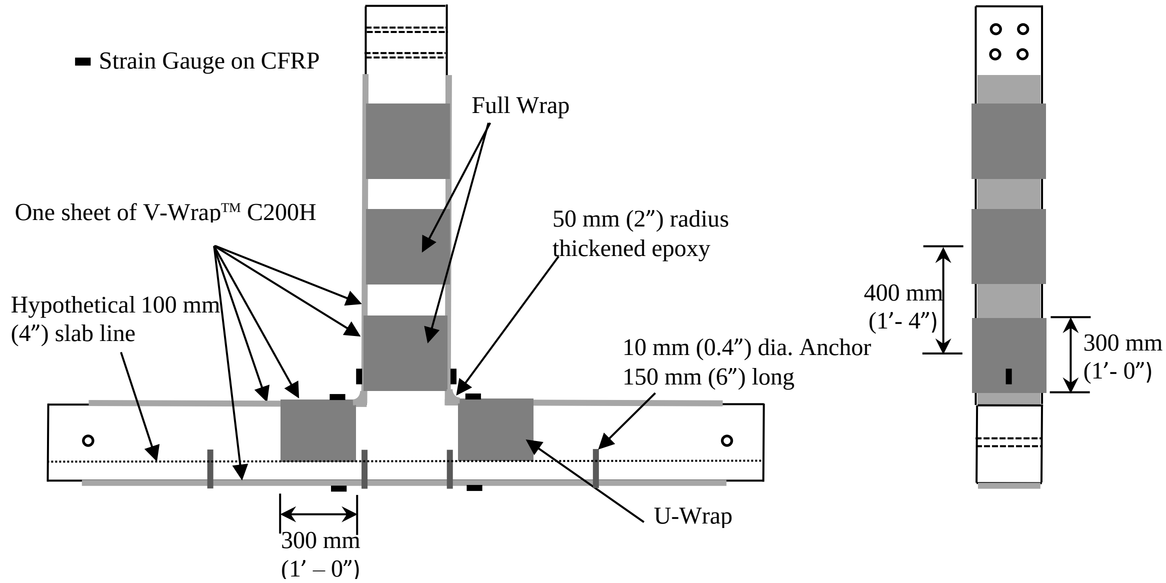

Figure 3.2. Strengthening Details and Strain Gauge Locations for Specimen BCA-2 (Saqan et al. 2020).

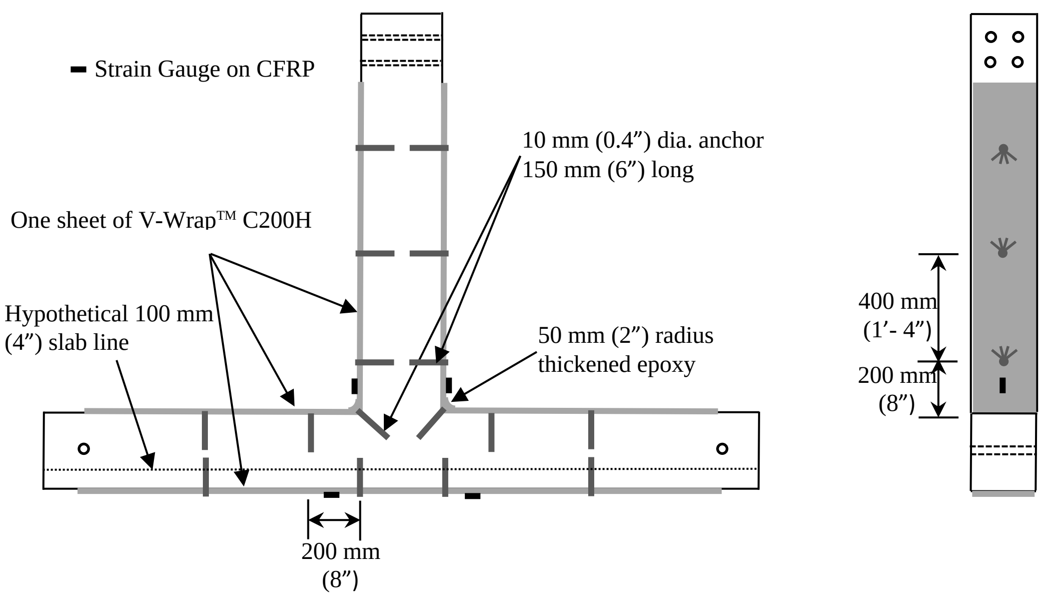

Figure 3.3. Strengthening Details and Strain Gauge Locations for Specimen BCA-3 (Saqan et al. 2020).

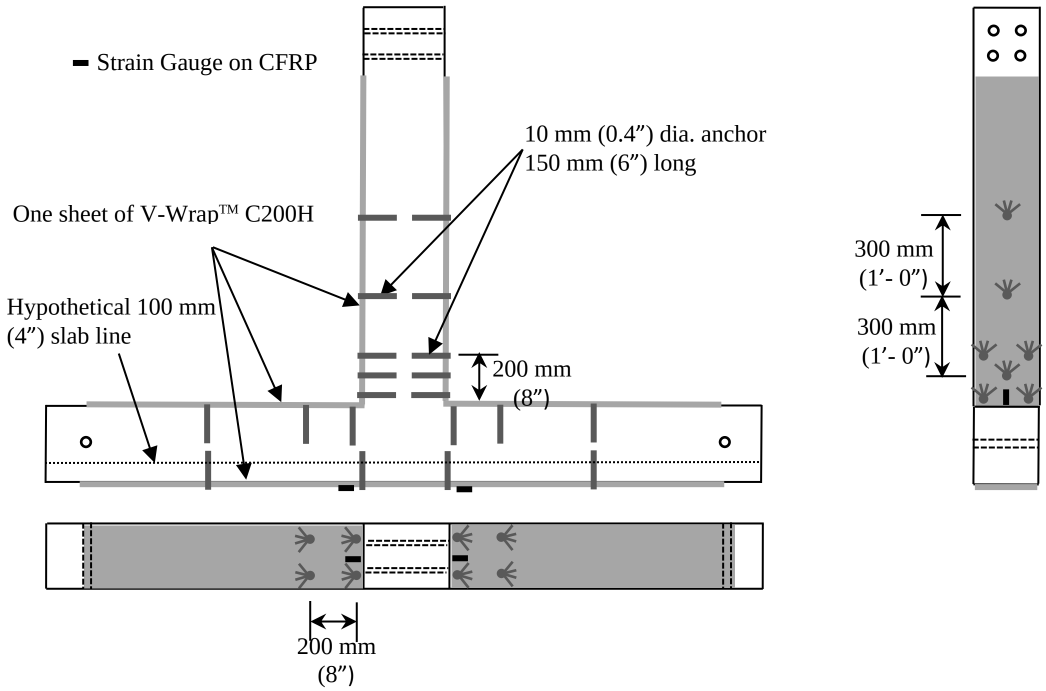

Figure 3.4. Strengthening Details and Strain Gauge Locations for Specimen BCA-4 (Saqan et al. 2020).

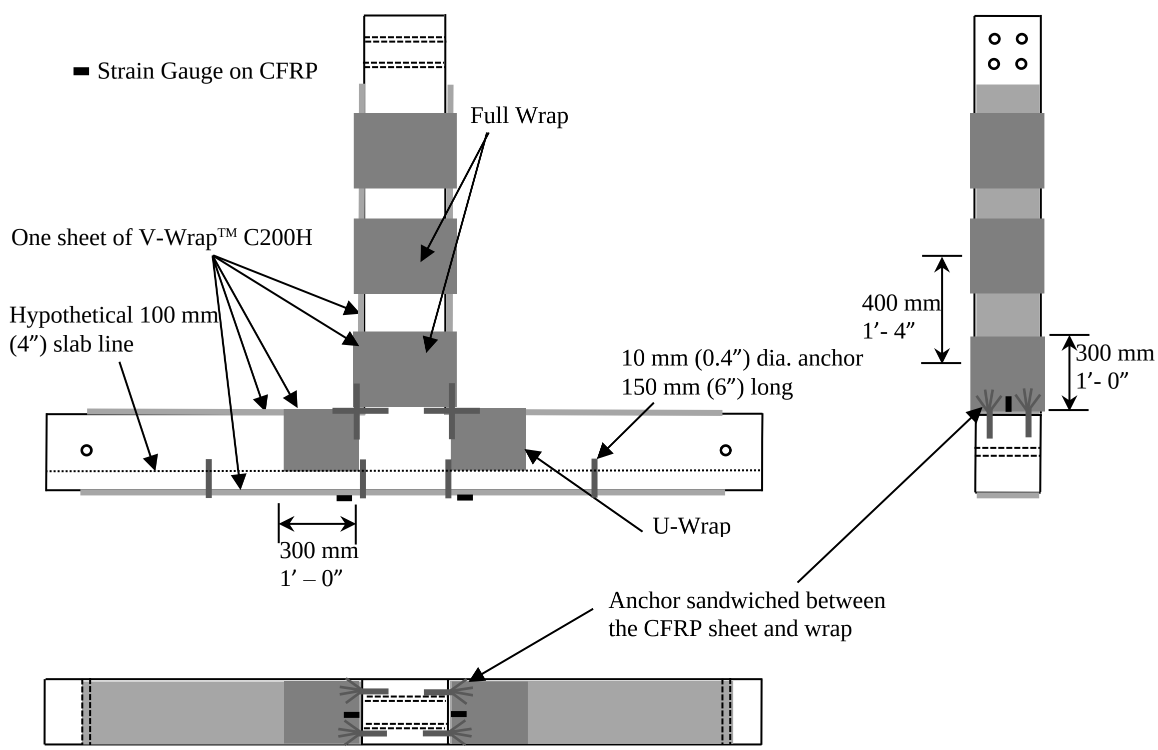

Figure 3.5. Strengthening Details and Strain Gauge Locations for Specimen BCA-5 (Saqan et al. 2020).

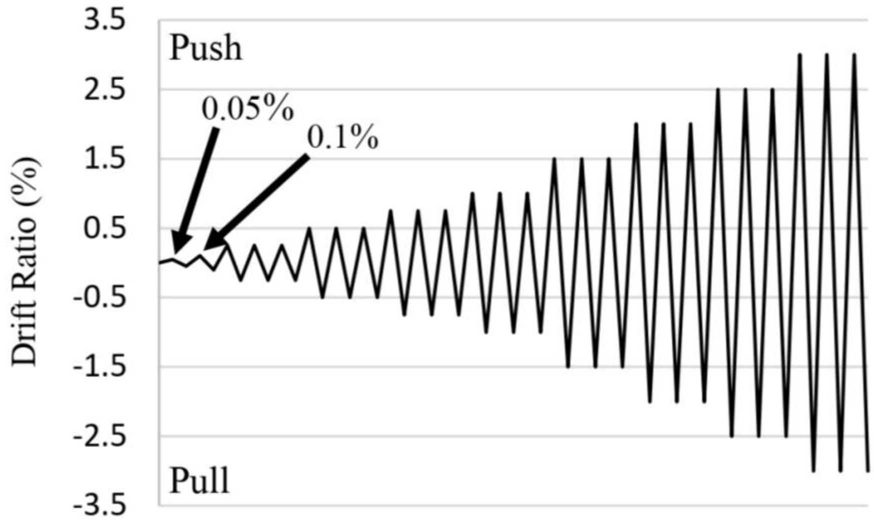

Figure 3.6. Displacement Loading Protocol (Saqan et al. 2020).

3-3 Analytical Model of Envelope Curve:

The trilinear approach developed by (Charkas et al. 2003) idealizes the moment-curvature behavior of reinforced concrete members using three distinct controlling parameters, the cracking, yielding and ultimate points. It, then, considers the varying flexural rigidity along the shear span and uses this notion to identify three distinct regions; the pre-cracking, post-cracking, and the post yielding zone in simply supported beams. These regions are the three linear curvature distributions that constitute the behavior of load-drift response of the vertical and horizontal parts of the specimens, Figure 3.7. By integrating the linear curvature function within each region, the deflection expression may be extended herein using the moment area theorems by superimposing the effect of both frame members in this study, Figure 3.8. This approach is applied to the four specimens strengthened with CFRP as referenced in the previous section to obtain the envelope response curve of the cyclic behavior. The envelope curve generated based on the trilinear approach is verified against the envelope curve obtained experimentally for all four specimens, as shown in Figure 3.9 through Figure 3.12. To specialize this approach to the specimens that are analyzed herein, the following equations are derived:

Vertical Member

The generalized nonlinear response of the vertical member admits the three distinct regions of pre-cracking, post-cracking, and post yielding, as shown in Figure 3.7. By integrating the moment of curvature distribution along the vertical member span, the tip deflection expression is obtained without considering the base rotation as follows:

Pre-cracking Region

$$\delta_1 = \int_0^{Lg} x\, \phi_{un}\ dx = \int_0^{Lg} x\ \frac{M(x)}{E_c I_g}\ dx \tag{1}$$

$$\delta_1 = \frac{PL_g^3}{3slope1} \tag{2}$$

Where:

$$slope1 = \frac{M_{cr}}{\emptyset_{cr}} \tag{3}$$

E_c= modulus of elasticity of concrete.

I_g= gross transformed section moment of inertia.

$$Lg = \frac{M_{cr}}{P} \tag{4}$$

ϕ_{un}= curvature corresponding to uncracking moment of section.

M_{cr}= cracking moment.

Post Cracking Region

$$\delta_2 = \int_{Lg}^{Ly} x\, \phi_{p-c}\ dx = \int_{Lg}^{Ly} x \left(\frac{(\emptyset_y - \emptyset_{cr})}{(\mathrm{M_y - M_{cr}})}\,(M - M_{cr}) + \emptyset_{cr}\right) dx = \int_{Lg}^{Ly} x \left(\frac{(\emptyset_y - \emptyset_{cr})}{(M_y - M_{cr})}\,(Px - M_{cr}) + \emptyset_{cr}\right) dx \tag{5}$$

$$\delta_2 = \frac{\emptyset_{Cr}}{2}\left(L_y^2 - L_g^2\right) + \frac{P\left(L_y^3 - L_g^3\right)}{3\ slope2} - \frac{M_{cr}\left(L_y^2 - L_g^2\right)}{2\ slope2} \quad (6)$$

Where:

$$slope2 = \frac{(M_y - M_{cr})}{(\emptyset_y - \emptyset_{cr})} \quad (7)$$

ϕ_{cr}= curvature corresponding to cracking moment of section.

ϕ_y= curvature corresponding to yielding moment of section.

$$Ly = \frac{M_y}{P} \quad (8)$$

M_y= moment corresponding to yielding of steel.

<u>Post Yielding Region</u>

$$\delta_3 = \int_{Ly}^{L_c} x\ \phi_{p-y}\ dx = \int_{Ly}^{L_c} x\ \left(\frac{(\emptyset_n - \emptyset_y)}{(M_n - M_y)}\left(M - M_y\right) + \emptyset_y\right) dx = \int_{Ly}^{L_c} x\ \left(\frac{(\emptyset_n - \emptyset_y)}{(M_n - M_y)}\left(Px - M_y\right) + \emptyset_y\right) dx \quad (9)$$

$$\delta_3 = \frac{\emptyset_y}{2}\left(L_c^2 - L_y^2\right) + \frac{P\left(L_c^2 - L_y^3\right)}{3\ slope3} - \frac{M_y\left(L_c^2 - L_y^2\right)}{2\ slope3} \quad (10)$$

Where:

$$slope3 = \frac{(M_n - M_y)}{(\emptyset_n - \emptyset_y)} \quad (11)$$

M_n= moment corresponding to ultimate moment of section.

ϕ_n= curvature corresponding to ultimate moment of section.

Lc= the length of the vertical member.

In the case of all three regions admitted, the tip deflection of deforming the vertical member is computed as follows:

$$\Delta_{fixed} = \delta_1 + \delta_2 + \delta_3 \tag{12}$$

Equation (12) above is universally applied for all loading levels. If the post-yielding region is absent, $\delta_3 = 0$ by setting $L_y = L_c$. Similarly, when the post-cracking region is absent, $\delta_3 = \delta_2 = 0$ by setting $L_g = L_y = L_c$.

Horizontal Members

Since the horizontal member receives half the moment at the base of the vertical member at the joint (two horizontal members share the moment), it is very unlikely for the post-yielding region to exist here, see Figure 3.8. Therefore, the rotation of the joint will add a rigid body deflection to the tip end at the applied load location, as follows:

$$\Delta_{tip} = \Delta_{fixed} + \theta_B L_c \tag{13}$$

Where:

$$\theta_B = \frac{t_{B/c}}{L_B} \tag{14}$$

L_B= half span of the horizontal member.

<u>Pre-cracking Region</u>

$$t_{B/c_1} = \int_0^{LgB} x\, \phi_{un}\ dx = \int_0^{LgB} x\, \frac{\emptyset_{cr}}{M_{cr}}\, M(x)\ dx = \int_0^{LgB} x\, \frac{\emptyset_{cr}}{M_{cr}}\, P_B\, x\, dx \tag{15}$$

Where:

$$P_B = \frac{M_a}{2L_{B,}},\ M_a = P\, L_c \tag{16}$$

$$t_{B/c_1} = \frac{P_B L_{gB}^3}{3slope1} \tag{17}$$

$$LgB = \frac{2M_{cr}}{M_a L_B} \tag{18}$$

<u>Post Cracking Region</u>

$$t_{B/c_2} = \int_{LgB}^{LB} x\,\phi_{p-c}\;dx = \int_{LgB}^{LB} x\,\left(\frac{(\emptyset_y - \emptyset_{cr})}{(M_y - M_{cr})}\,(M(x) - M_{cr}) + \emptyset_{cr}\right)\,dx =$$

$$\int_{LgB}^{LB} x\,\left(\frac{(\emptyset_y - \emptyset_{cr})}{(M_y - M_{cr})}\,(P_B x - M_{cr}) + \emptyset_{cr}\right)\,dx \tag{19}$$

$$t_{B/c_2} = \frac{\emptyset_{Cr}}{2}\left(L_B^2 - L_{gB}^2\right) + \frac{P_B\left(L_B^3 - L_{gB}^3\right)}{3\;slope1} - \frac{M_{cr}\left(L_B^2 - L_{gB}^2\right)}{2\;slope1} \tag{20}$$

Where:

$$\theta_B = \frac{t_{B/c_1} + t_{B/c_2}}{L_B} = \frac{P_B L_{gB}^3}{3slope1L_B} + \frac{\emptyset_{Cr}}{2L_B}\left(L_B^2 - L_{gB}^2\right) + \frac{P_B\left(L_B^3 - L_{gB}^3\right)}{3\;slope1L_B} - \frac{M_{cr}\left(L_B^2 - L_{gB}^2\right)}{2\;slope1L_B} \tag{21}$$

Equation (20) above is universally applied for all loading levels. If the post-cracking region is absent, $t_{B/c_2} = 0$ by setting $L_{gB} = L_B$.

It is worth mentioning here that the lateral force on the tip of the vertical member produces a small axial compression on the left horizontal member and a small axial tension on the right horizontal member. These axial forces are ignored in this formulation when determining the tip deflection since they are small enough to alter the moment-curvature response of the horizontal member.

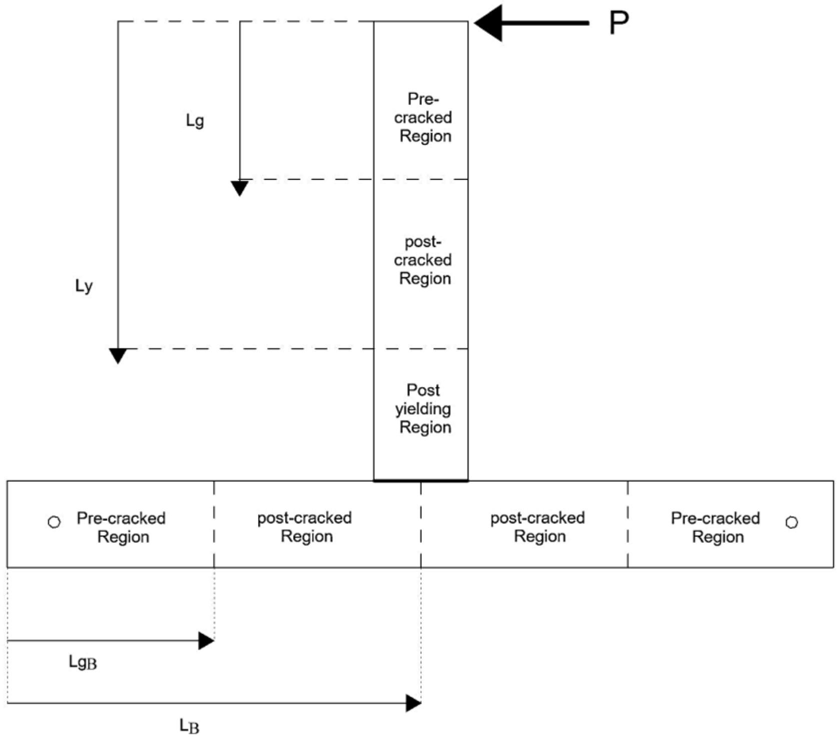

Figure 3.7. The Various Moment-Curvature Regions Generalized for The RC Frame.

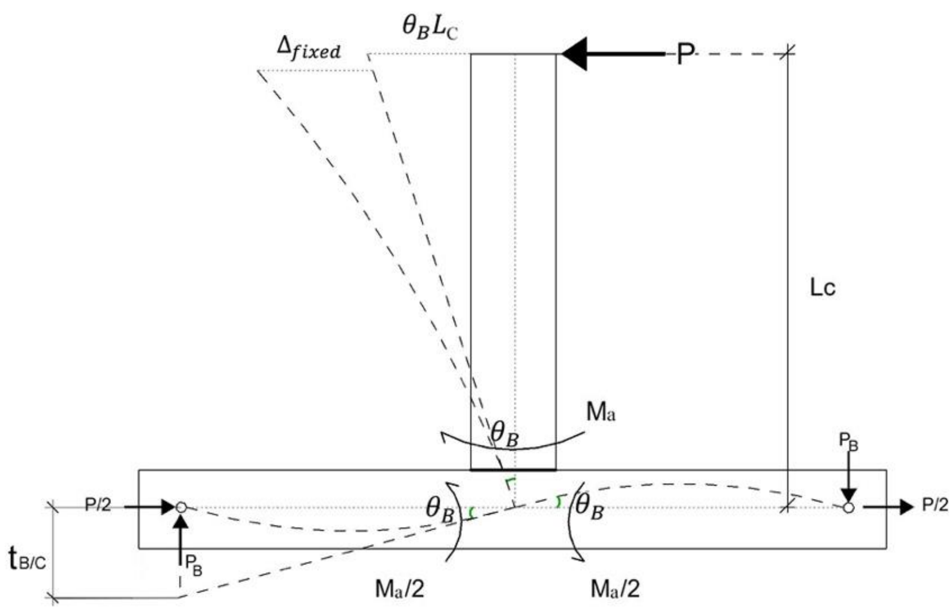

Figure 3.8. Adjustment of Total Column Drift by The Addition of Joint Rotation.

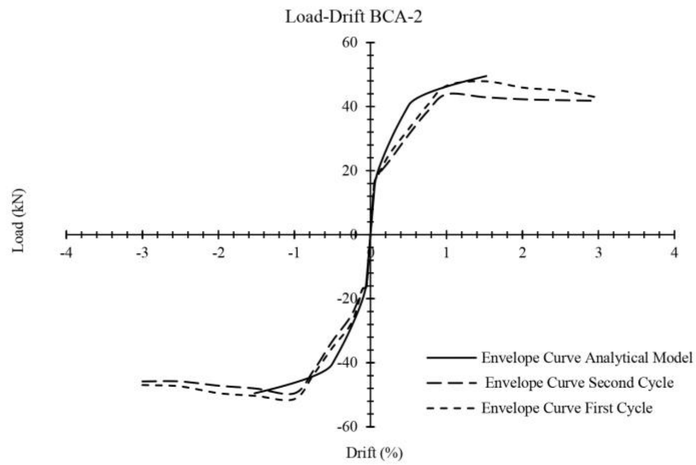

Figure 3.9. The Trilinear Load-Deflection Analytical VS Experimental Results Specimen BCA-2 (1 Kips=4.45 KN).

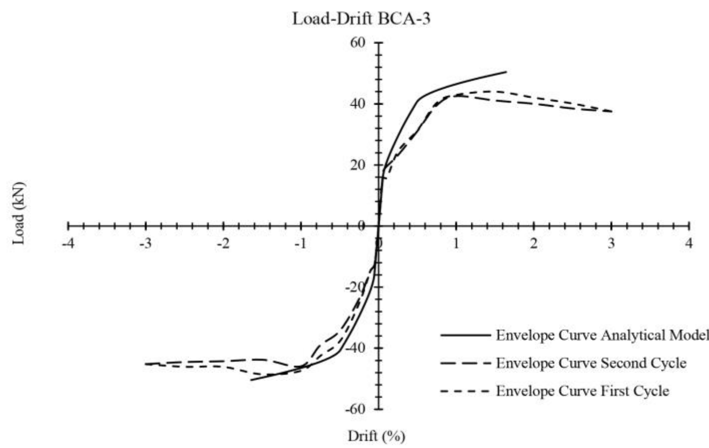

Figure 3.10. The Trilinear Load-Deflection Analytical VS Experimental Results Specimen BCA-3 (1 Kips=4.45 KN).

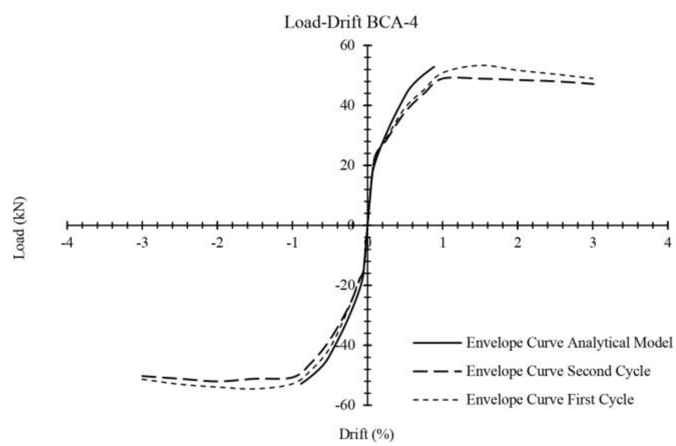

Figure 3.11. The Trilinear Load-Deflection Analytical VS Experimental Results Specimen BCA-4 (1 Kips=4.45 KN).

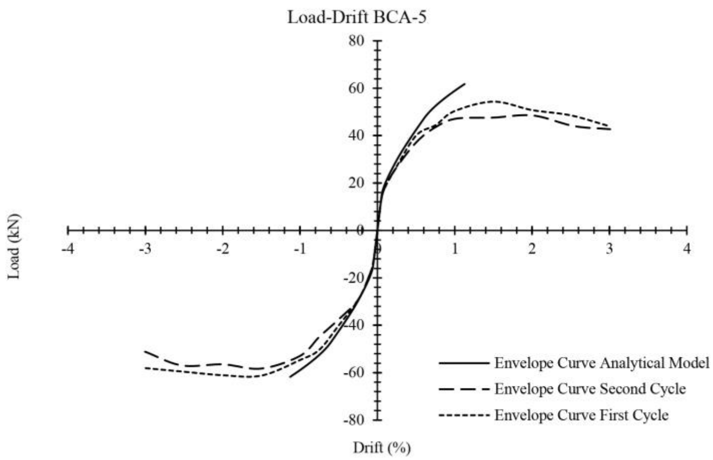

Figure 3.12. The Trilinear Load-Deflection Analytical VS Experimental Results Specimen BCA-5 (1 Kips=4.45 KN).

3-4 Hysteresis Loops Model:

When modeling the hysteresis loops, each cycle is broken down into three linear regions in the unloading and reloading paths, respectively. These linear regions are named push, inflection range, and pull side in the unloading path as well as the reloading path, see Figure 3.13. It is observed that the unloading push path has a very similar slope to the reloading pull path. Accordingly, these two-line slopes are averaged together in the present model and are referred to as Region A, Figure 3.14. Similarly, the unloading pull path has a comparable slope to the reloading push path, and they are, therefore, averaged together in this model and referred to as Region C, Figure 3.14. Also, the inflection range, indicated as Region B, has similar slopes in the unloading and reloading bounds. Therefore, these two bounds are averaged here as well. To automate the model, curves correlating the ratio of unloading and reloading push slope variations to the initial backbone curve slope on the x-axis vs. the backbone curve drift ratios at the envelop curve to that drift ratio at yielding on the y-axis are generated for all cycles throughout the response, Figure 3.15. These three curves define the rules that the hysteresis loops behave in accordance with. For example, the drift ratio of the yielding point on the envelope curve (100%

value of the y-axis) corresponds to a 0.24 slope ratio for region A, 0.1 slope ratio for region B and 0.18 slope ratio for region C, Figure 3.15. This formulation is used consistently for all cycles of load-drift ratio when reconstructing the hysteresis loops of specimen BCA-2. Likewise, specimen BCA-4 has similar graphs developed for that calibration in Figure 3.16. Finally, the three-line slopes extracted from Figure 3.15 or Figure 3.16 extend to drift ratio pivot points (on the drift axis) based on the following equations, Figure 3.13 and Figure 3.14:

$$d_{push-Un} = d_{pull-Re} = 25\%\ of\ d_{cy-Un} \tag{22}$$

$$d_{ir-Un} = d_{ir-Re} = 50\%\ of\ d_{cy-Un} \tag{23}$$

$$d_{push-Re} = d_{pull-Un} = 25\%\ of\ d_{cy-Un} \tag{24}$$

Where:

$d_{push-Un}$ *is* Unloading push side shift on the x – axis (drift axis) of the hysterisis loop.

$d_{pull-Re}$ *is* Reloading pull side shift on the x – axis (drift axis) of the hysterisis loop.

d_{cy-Un} *is* the total drift width on the x – axis (drift axis) of the hysterisis loop.

d_{ir-Un} *is* Unloading Inflection range shift along the x – axis (drift axis) of the hysterisis loop.

d_{ir-Re} *is* Reloading Inflection range shift along the x – axis (drift axis) of the hysterisis loop.

$d_{pull-Un}$ *is* Unloading pull side shift along the x – axis (drift axis) of the hysterisis loop.

$d_{push-Re}$ *is* Reloading push side shift along the x – axis (drift axis) of the hysterisis loop.

By using these formulations, the hysteresis loop responses of specimens BCA-2 and BCA-4 were accurately reconstructed for the entire cyclic loading range.

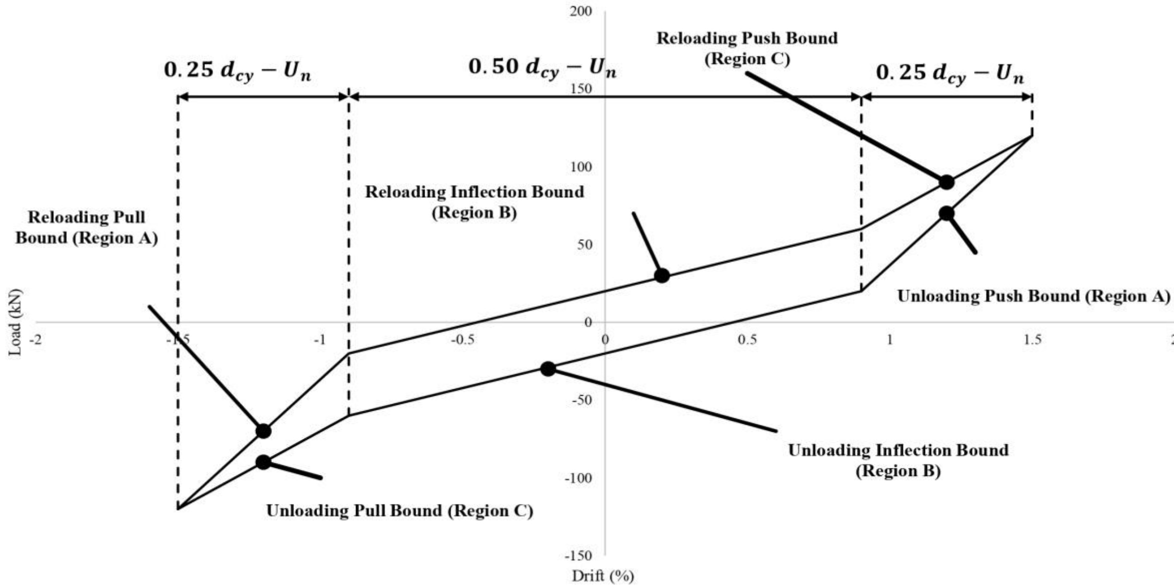

Figure 3.13. Three Linear Regions of The Hysteresis Loop Model.

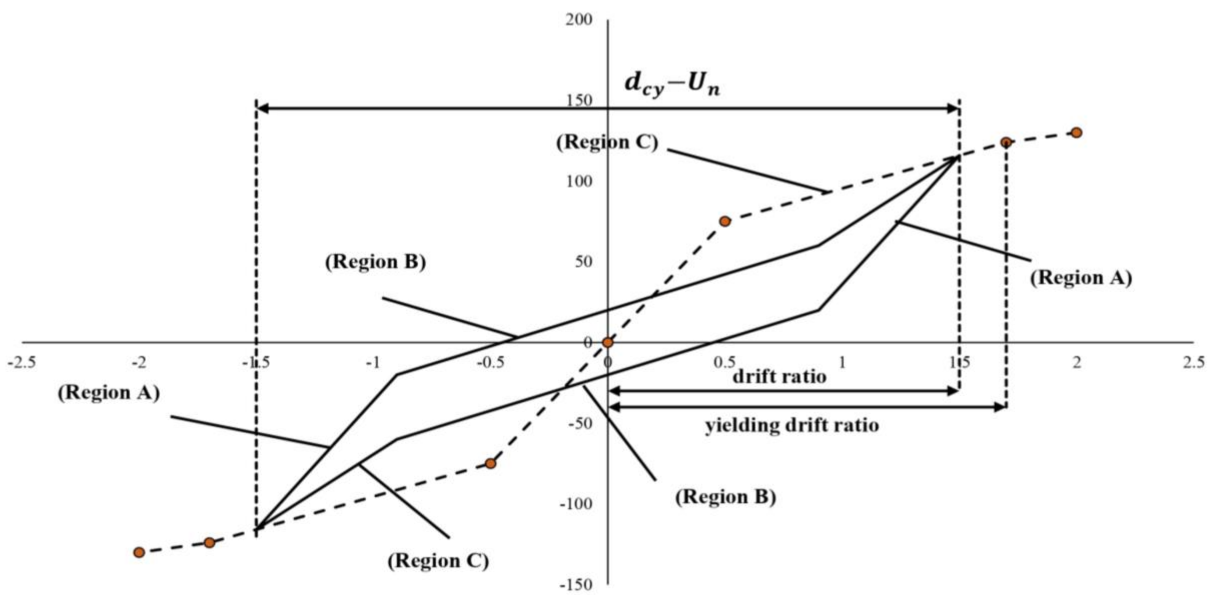

Figure 3.14. Hysteresis Regions Relative to The Backbone Curve.

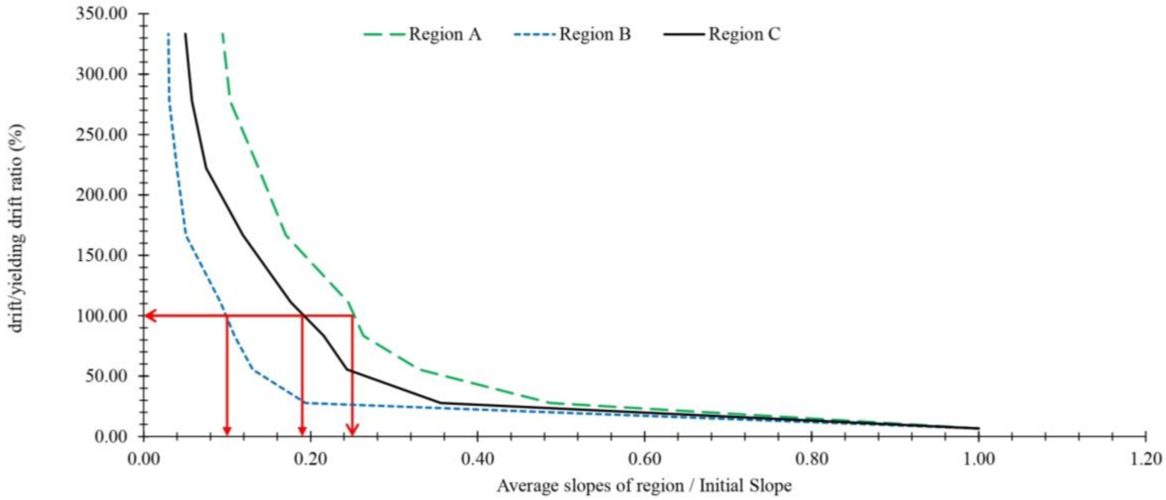

Figure 3.15. Regions A, B, C Graphs to Characterize the Hysteresis Loops Specimen BCA-2.

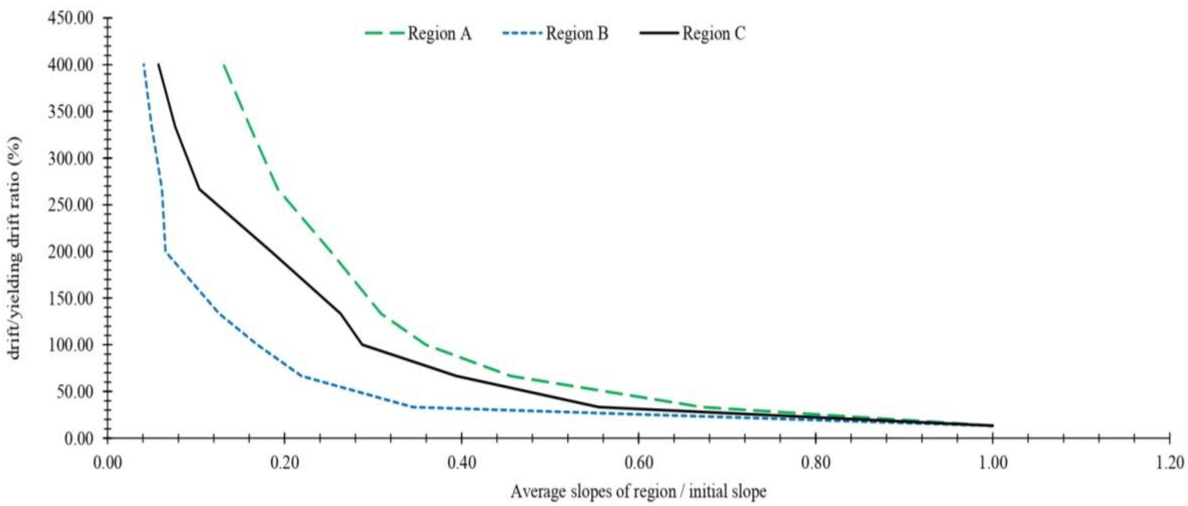

Figure 3.16. Regions A, B, C Graphs to Characterize the Hysteresis Loops Specimen BCA-4.

3-5 Analysis Steps:

The synthesis of the hysteresis loops can be re-produced based on the following steps for a single hysteretic cycle:

1. Identify the departure point from the envelope curve of the load-deflection response on the push side, which is assumed on average to be similar to that on the pull side.
2. Use Figure 3.15 or Figure 3.16 to extract the slope of the unloading line on the push side, which is the same as the reloading line of the pull side (region A), see Figure 3.13.

3. Use Figure 3.15 or Figure 3.16 to extract the slope of the inflection unloading bound on the push side, which is the same as the inflection reloading bound of the pull side (region B), see Figure 3.13.
4. Use Figure 3.15 or Figure 3.16 to extract the slope of the unloading push bound, which is the same as the reloading pull bound (region C), see Figure 3.13.
5. Define the boundaries of each region using vertical lines drawn at the inflection points shown in Figure 3.13.

3-6 Results and Verification:

Envelope Curve Results

The experimental results, reported in reference (Saqan et al. 2020), are compared to the analytical results which are calculated based on the modified trilinear model as discussed in equations 1-20, using Microsoft Excel. Table 3-4 shows the experimental results as well as the calculated results at cracking, yielding, and ultimate debonding failure stages for all four specimens.

It is evident that there are slight variations between the two sets of data when comparing the analytical loads to the experimental results. Generally, the analytical cracking loads tend to underestimate the values obtained experimentally, while the yielding loads show closer agreement. Additionally, the ultimate loads obtained analytically for all specimens are in good agreement with the experimental values. These variations can be attributed to several factors, including assumptions about the material behavior, and the analytical model simplification. Figure 3.9 to Figure *3.12* illustrate the comparison between the analytical solutions and the experimental results for all specimens.

Table 3-4 Comparison of Analytical and Experimental Results.

Specimen	Experimental results			Analytical results		
	Cracking load, KN (kips)	Yielding load, KN (kips)	Average ultimate load, KN (kips)	Cracking load, KN (kips)	Yielding load, KN (kips)	Ultimate load, KN (kips)
BCA-2	18.5 (4.16)	37.9 (8.52)	48.8 (10.97)	15.12 (3.40)	40.44 (9.09)	49.60 (11.15)
BCA-3	17.8 (4.00)	37.4 (8.41)	46.5 (10.45)	15.79 (3.55)	40.52 (9.11)	50.41 (11.33)
BCA-4	23.0 (5.17)	47.5 (10.68)	53.93 (12.12)	15.74 (3.54)	44.00 (9.89)	52.86 (11.88)
BCA-5	20.0 (4.50)	47.79 (10.77)	58.75 (13.20)	14.65 (3.29)	47.275 (10.63)	61.715 (13.87)

Hysteresis Loop Results

Model Calibration

The hysteresis model rules, developed herein based on the phenomenological formulation of RC frame assemblies strengthened with CFRP, produced a load-drift ratio hysteresis loop curves using the data in Figure 3.15 and Figure 3.16 Therefore, the hysteresis loops of specimen BCA-2 were derived based on the slope variations in Figure 3.15 resulting in good agreement to the ones obtained experimentally as reflected in Figure 3.17. It can be observed that the hysteresis loops in the post-cracking region show excellent correspondence to the experimental loops while the analytical loops in the post-yielding region reflect a very slight deviation. To further clarify the illustration of the analytical hysteresis loops, they are plotted against the experimental envelope curve in Figure 3.18. Similarly, the hysteresis loops of specimen BCA-4 were derived based on the slope variations in Figure 3.16 resulting in good agreement to the ones obtained experimentally as reflected in Figure 3.19. It can also be observed that the hysteresis loops in the post-cracking region show excellent correspondence to the experimental loops while the analytical loops in the post-yielding region reflect a very slight deviation. To further clarify the illustration of the analytical hysteresis loops, they are plotted against the experimental envelope curve in Figure 3.20.

Model Verification

The hysteretic behavior model used to predict the hysteresis loops is then used to predict its blind applicability on other sets of experimental data. For this purpose, the load-drift ratio for BCA-3 and BCA-5 are used to compare against the phenomenological predictions of BCA-2 and BCA-4 from Figure 3.15 and Figure 3.16, respectively. Accordingly, the present phenomenological model is benchmarked against other experiments sharing general features but not the exact same anchorage patterns in order to validate its applicability to other specimen results.

BCA-3

It is worth mentioning that the specimens BCA-2 and BCA-3 share similar general CFRP anchorage layout features. Therefore, the lack of anchorage in the critical joint section just below the CFRP at the beams top surface is considered here in the moment-curvature analysis as an absent CFRP strengthening of that critical section. The load-drift ratio data taken experimentally were applied to the phenomenological predictions made for BCA-2 and the results obtained were in excellent agreement with those of specimen BCA-3 as reflected in Figure 3.21. It can be observed that the analytical loops show excellent correspondence to the experimental ones in the post-cracking region while they reflect very slight shifts in the post-yielding region.

BCA-5

It should also be noted that specimens BCA-4 and BCA-5 share similar general CFRP anchor layout features. Therefore, the anchor embedded past the sheet location that strengthens the beams top surface is considered here in the moment-curvature analysis as a present CFRP flexural reinforcement represented by the embedded anchor relative to the vertical member response. Similarly, the experimental load-drift data for specimen BCA-5 were applied to the phenomenological prediction model made for BCA-4 and the results obtained were in excellent agreement as reflected in Figure 3.22. It is evident that the analytical loops show excellent correspondence to the experimental ones in the post-cracking region while they reflect very slight shifts in the post-yielding region.

Thus, it can be concluded that the phenomenological assumptions made to calibrate the hysteresis loops can be employed successfully to predict the hysteretic behavior of similarly strengthened and anchored specimens.

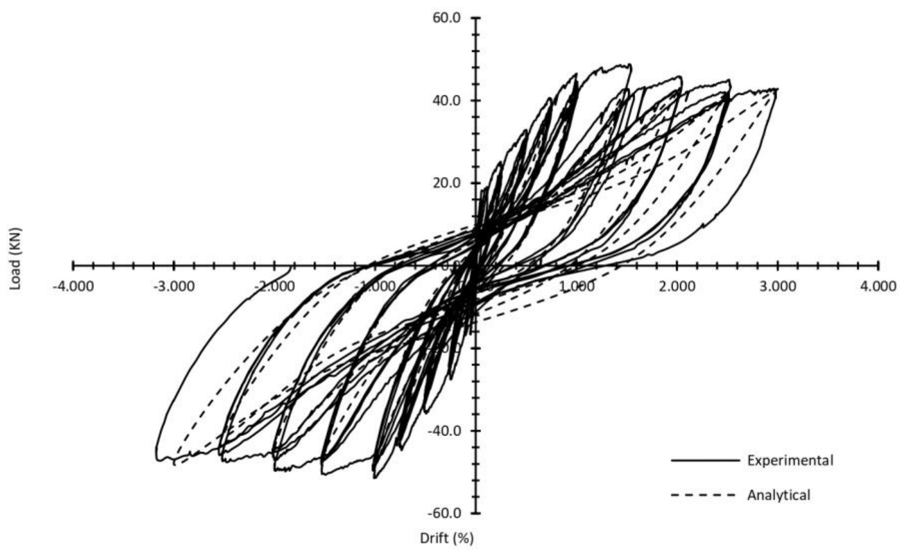

Figure 3.17— Calibration of Hysteresis Loops Experimental VS Analytical Specimen BCA-2 (1 Kips=4.45 KN).

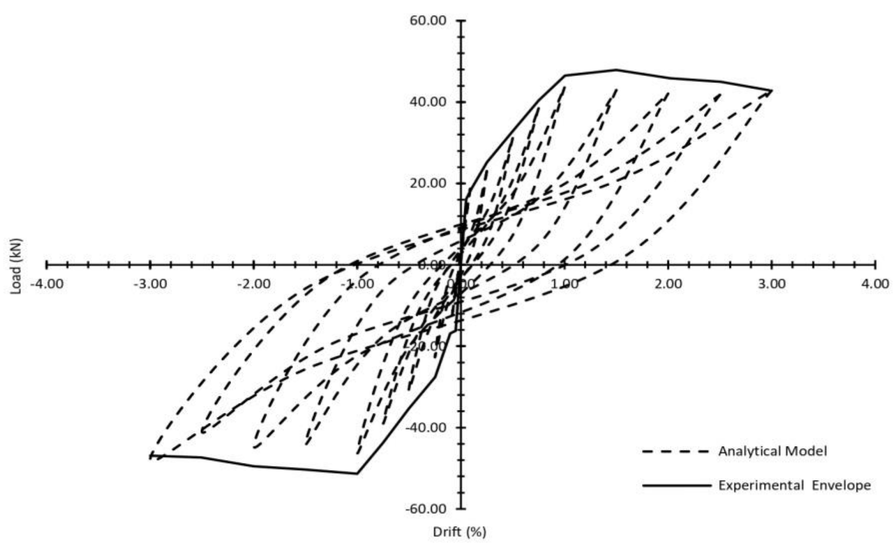

Figure 3.18. Calibration of Modeled Hysteresis Loops VS Experimental Envelope Curve Specimen BCA-2 (1 Kips=4.45 KN).

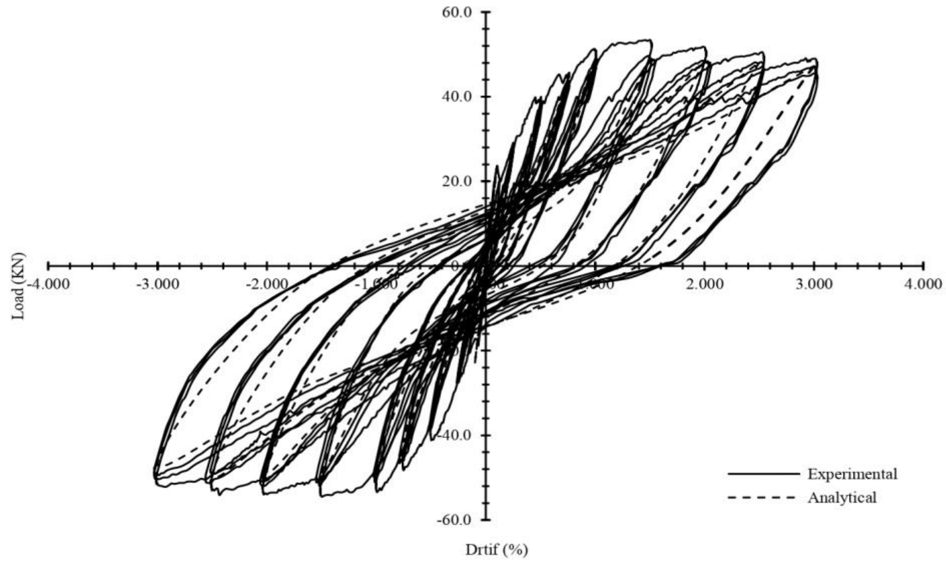

Figure 3.19. Calibration of Hysteresis Loops Experimental VS Analytical Specimen BCA-4 (1 Kips=4.45 KN).

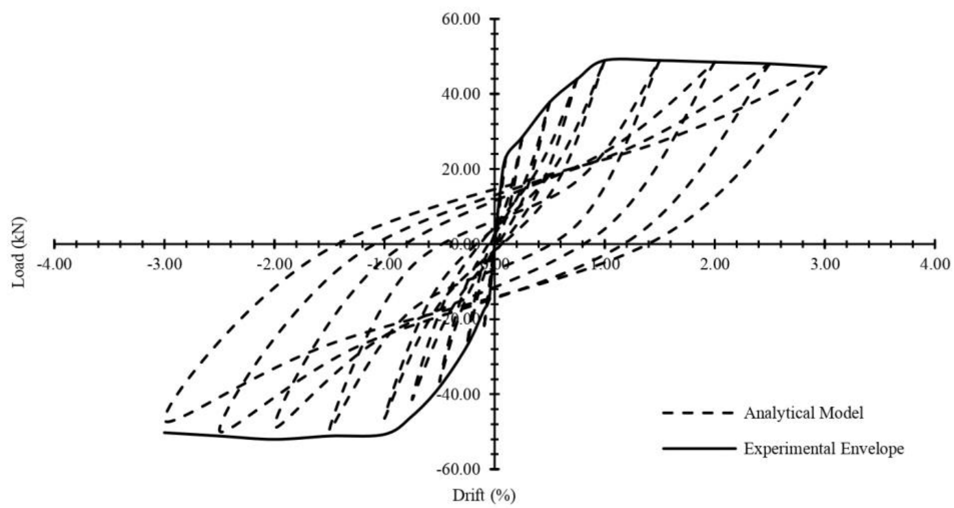

Figure 3.20. Calibration of Modeled Hysteresis Loops VS Experimental Envelope Curve Specimen BCA-4 (1 Kips=4.45 KN).

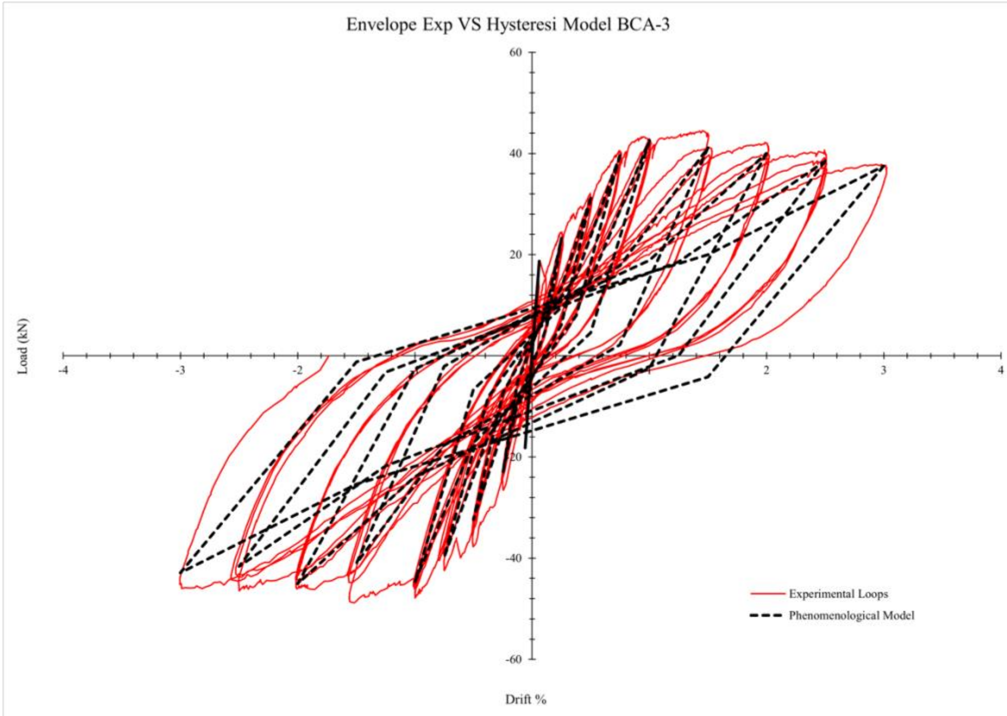

Figure 3.21. Both Experimental and Modeled Hysteresis Loops Against Experimental Envelope Curve Specimen BCA-3 (1 Kips=4.45 KN).

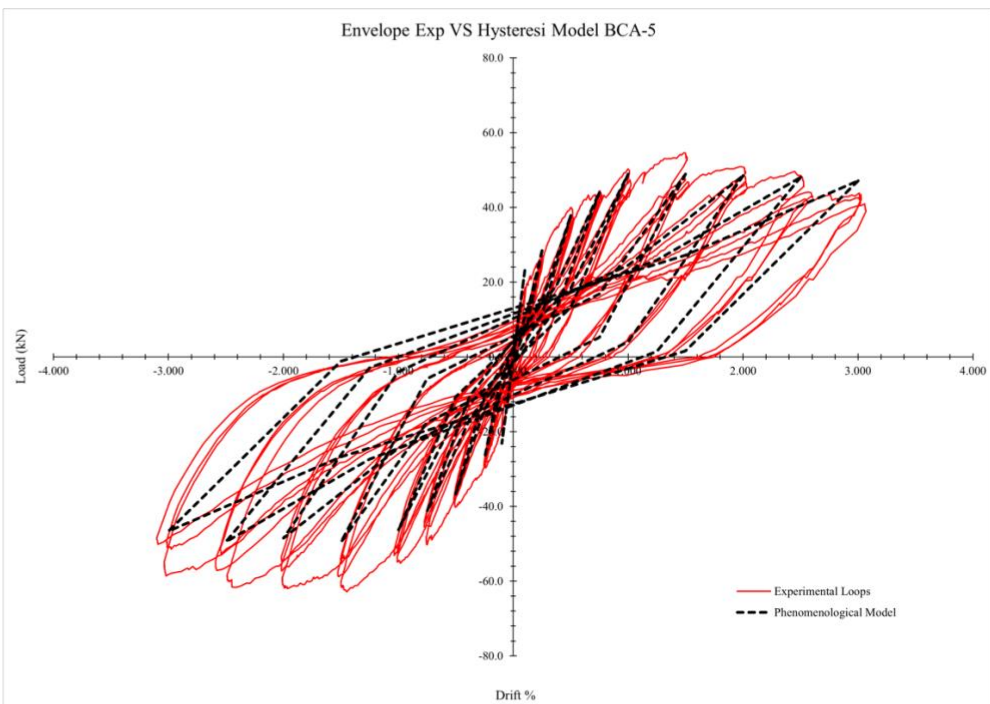

Figure 3.22. Both Experimental and Modeled Hysteresis Loops Against Experimental Envelope Curve Specimen BCA-5 (1 Kips=4.45 KN).

3-7 Summary and Conclusion

In this study, a trilinear moment curvature approach, developed by (Charkas et al. 2003), is extended to determine the full nonlinear load-deflection response for reinforced concrete frame assemblies strengthened with CFRP. The treatment yielded closed-form deflection expressions for the envelop curves of the cyclic response of these assemblies. Excellent agreement was observed between the envelope curves developed for these frame assemblies and the experimental envelope curves. Furthermore, a phenomenological hysteretic load-deflection model is postulated in this work using observations of the experimental hysteresis loops for two frame assemblies to calibrate the key parameters controlling the model layout. It was observed that hysteresis loops were very accurately depicted by applying a three-region model while building master curves for the degradation in the slopes of these regions as the load increases. Furthermore, it was noted that the drift span within each cycle can be made of 25%-50%-25% of the entire cycle drift range for the unloading-inflection-reloading regions, which was implemented as an integral part of the current model. This model was applied to two other frame assemblies sharing similar strengthening features to those used in model calibration illustrating excellent correspondence after blind comparisons. The verifications performed reflect very good promise for this model in capturing the shape of the envelope curve as well as the hysteresis loops at different levels of loading, which may be easily extended to other structural systems. Being a phenomenological hysteresis model, it may be only possible to extend to other structural systems and applications after some general or basic modifications or improvements. This is anticipated to be true for almost all models built upon experimental data.

CHAPTER 4: ANALYTICAL MODEL OF CONCRETE CYCLIC BEHAVIOR IN TENSION AND IN COMPRESSION

4-1 Introduction:

The analysis of concrete cyclic behavior under both tension and compression is fundamental to comprehending the stress and strain patterns exhibited in a frame structure throughout various stages within a single hysteresis loop. In pursuit of this objective, a comprehensive model derived from experimental data in literature is introduced in this chapter that studies the behavior of concrete in cyclic compression and cyclic tension. The phenomenological model proposed herein predicts the stresses and strains of concrete on the envelope curve, the lines along which the stresses and strains at unloading inflection occurs, and the residual strain values under cyclic compressive loading and cyclic tensile loading. The chapter further explores the applicability of the model in reverse cyclic loading condition by tailoring it with the trilinear approach proposed by Rasheed et al (2013), and the analytical model originally formulated by Mansour and Hsu (2005) that delineates unloading and reloading stress-strain domains which are a function of the envelope tensile strain and confined within the bounds of the envelope curve as seen in Figure 4.1. Therefore, this chapter studies different cyclic conditions, combining them with the existing models to propose new phenomenological models acquiring the unique behavior of concrete stress-strain relationship at different strain levels for both the envelope and cyclic response.

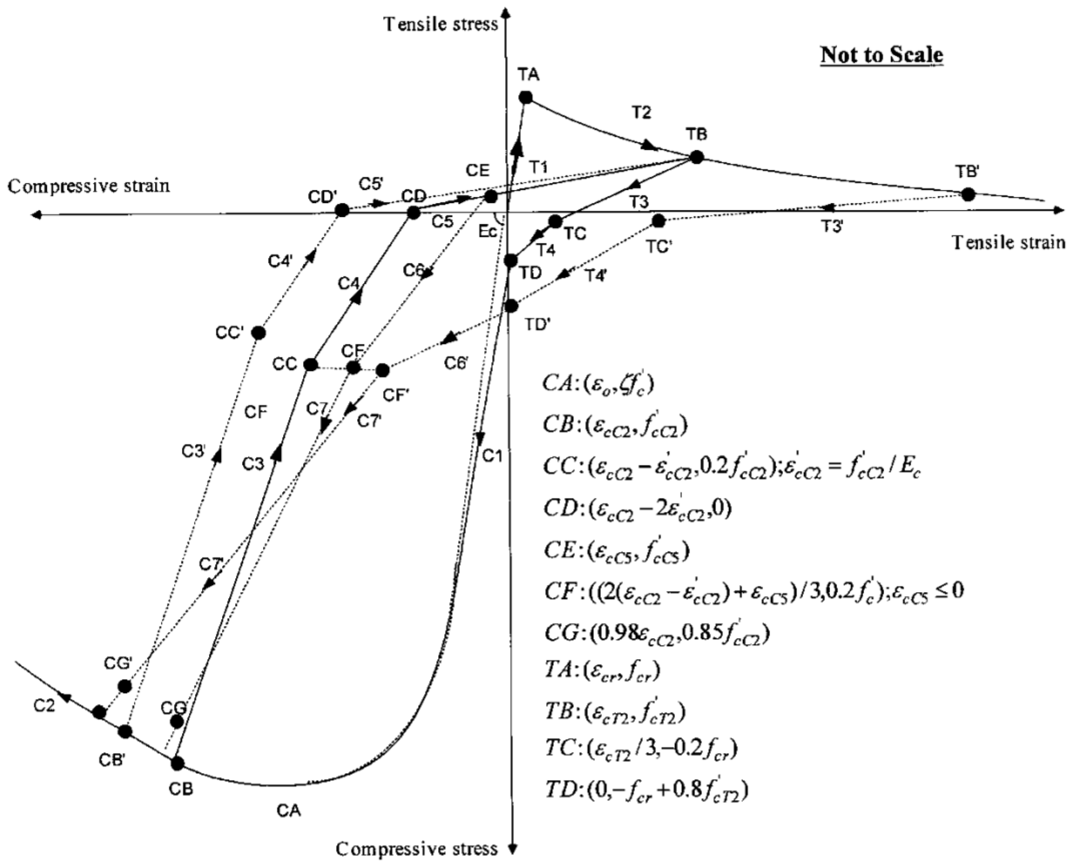

Figure 4.1. Analytical Model for Cyclic Stress-strain Curves of Concrete (Mansour and Hsu 2005).

4-2 Concrete Behavior Under Cyclic Compressive Loading:

For plain concrete in cyclic compressive loading, the envelope curve is divided into two regions: the pre-peak and post-peak regions. the first is a curve defined by three strain values, the zero strain, the strain corresponding to 0.45 f'c, and the strain corresponding to f'c. The post peak region that defines the softening is simplified as a linear curve and occurs between the normalized compressive strain value (1.0) and the normalized ultimate strain value (2.5). Another important observation that was drawn from the experimental data indicates that the inflection points for every compressive cycle is observed to fall on a line that starts at a normalized stress of 0.4 corresponding to a normalized strain of zero and linearly descends to a normalized stress of zero corresponding to a normalized strain of 2.50, as shown in Figure 4.2. Based on the following observations, a model is calibrated as follows:

Model Calibration:

The current model is based on experimental observations from available data. Based on these observations, the following assumptions were made:

1- The coordinate of the pivot point at which all of the unloading paths intersect if extended linearly is at (-0.35, -1.50).

2- The coordinate of the pivot point at which all of the reloading paths intersect if extended linearly is at (-0.35, -0.80).

3- The inflection point on the unloading path is assumed to lie along a diagonal line between the two points (0.00, 0.40) and (2.50, 0.00), as shown in Figure 4.2.

- **Envelope curve:**

Equation (25)-(27) can be used to estimate the envelope curve as follows:

For $0.00 \leq \frac{\varepsilon_c}{\varepsilon'_c} \leq \frac{5.0}{19}$:

$$\frac{\sigma}{f'_c} = 1.71\frac{\varepsilon_c}{\varepsilon'_c} \tag{25}$$

For $\frac{5.0}{19} \leq \frac{\varepsilon_c}{\varepsilon'_c} \leq 1.00$:

$$\frac{\sigma}{f'_c} = 0.0216987 + 1.810073\frac{\varepsilon_c}{\varepsilon'_c} - 0.8317718\left(\frac{\varepsilon_c}{\varepsilon'_c}\right)^2 \tag{26}$$

For $1.00 \leq \frac{\varepsilon_c}{\varepsilon'_c} \leq 2.50$:

$$\frac{\sigma}{f'_c} = -0.413\frac{\varepsilon_c}{\varepsilon'_c} + 1.413 \tag{27}$$

- **Unloading path:**

The slope of any unloading path can be calculated using Equation (28):

$$S_u = \frac{y_e + 1.5}{x_e + 0.35} \qquad (28)$$

Where:

y_e and x_e are the departure point on the envelope curve.

S_u is the slope of the unloading path.

- **Reloading path:**

The slope of any reloading path can be calculated using Equation (29):

$$S_R = \frac{y_e + 0.80}{x_e + 0.35} \qquad (29)$$

Where:

y_e and x_e are the departure point on the envelope curve.

S_R is the slope of the reloading path.

To locate the coordinate of the x intercept of any reloading path, Equation (30) can be used:

$$x_{int} = \frac{-0.35\, S_R + 0.80}{S_R} \qquad (30)$$

- **Inflection point:**

The inflection point can be determined by the intersection of the unloading line and the descending inflection line leading to, Equations (31) and (32):

$$x_i = \frac{0.35\, S_u - 1.90}{-0.16 - S_u} \qquad (31)$$

$$y_i = -0.16\, x_i + 0.40 \qquad (32)$$

After developing all the necessary equations, the model was calibrated against the original experimental data to verify its accuracy. The results are presented in Figure 4.3. Further validation was conducted to assess the applicability of the present model in other experiments, as explained in the next section.

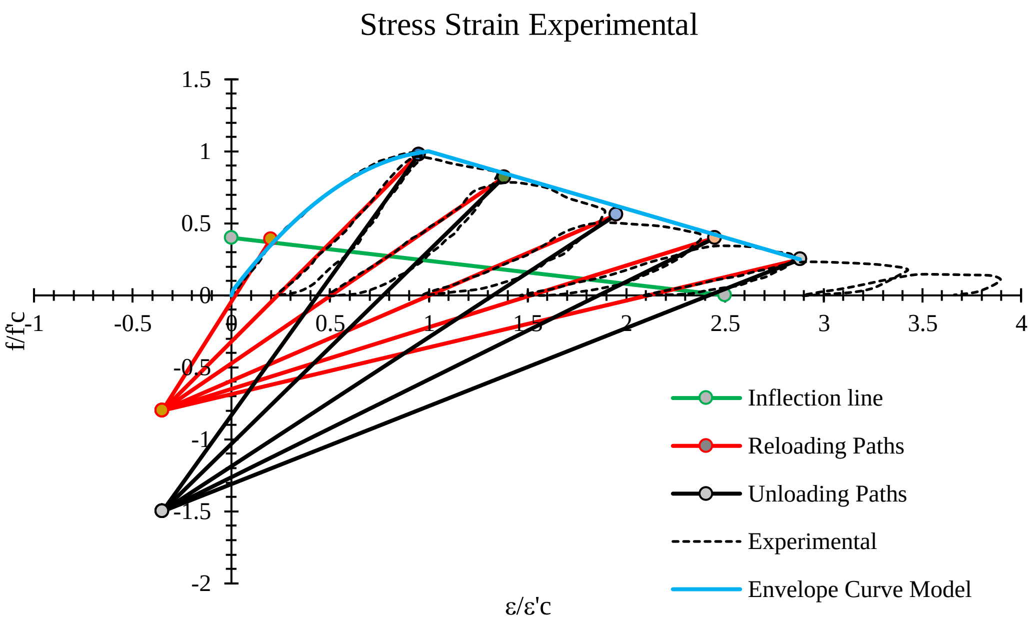

Figure 4.2. Unloading and Reloading Slopes Intersection Points for Cyclic Compression Loading.

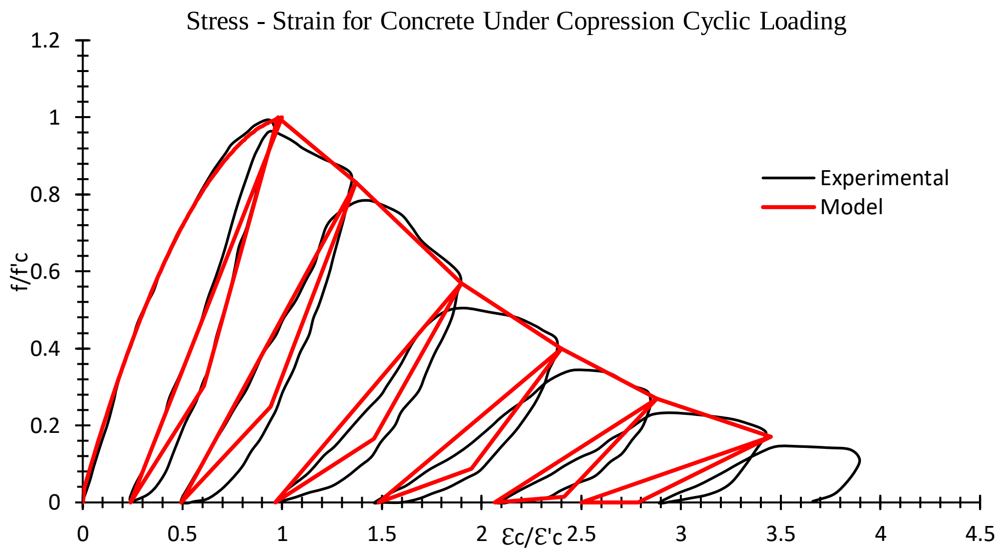

Figure 4.3.Model Calibration from Experimental Data.

Model verification:

The comparison results between the present model and the original experimental data demonstrate a very good agreement, leading to the conclusion that the developed model effectively represents the behavior of plain concrete under cyclic compression loads. Figure 4.4 and Figure 4.5 illustrate the comparison results between the current model and the available experimental data.

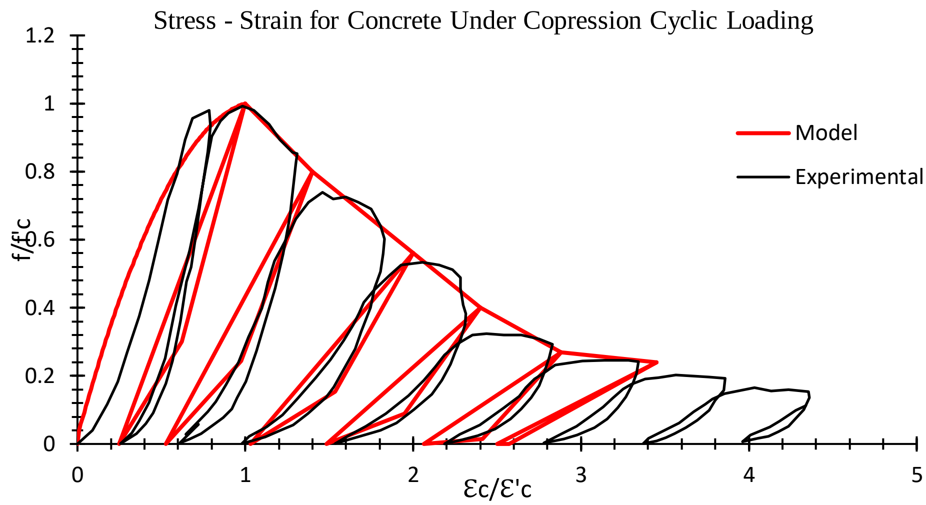

Figure 4.4.Model Verification from Experimental data No.1.

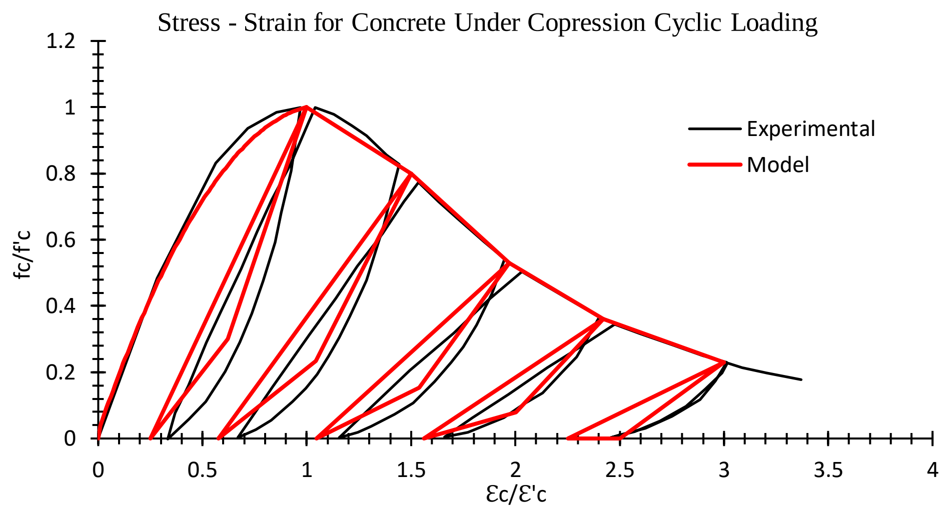

Figure 4.5.Model Verification from Experimental Data No.2.

4-3 Concrete Behavior Under Cyclic Tensile Loading:

For plain concrete in cyclic tensile loading, most researchers have used an approach at which the pre-peak region has a linear elastic relationship that represents well the behavior of concrete in tension. However, in the post peak region, different researchers have adopted and proposed different models for the softening descending behavior. One of the adopted studies in this work is proposed by Abouelleil and Rasheed (2021) in which the softening branch in the post peak region abruptly drops from the normalized tensile stress level to half that amount immediately upon cracking. Then it assumes a linear degradation to a strain level equal to 1.4 times the yielding normalized strain of the reinforcing steel. Another adopted model proposed by Nayal and Rasheed (2006) suggests an abrupt change from the normalized tensile stress level to 0.8 that value upon cracking. The post peak region then descends further to ten times the cracking strain. The model proposed herein for the cyclic tensile behavior of plain concrete is based on a hybrid version of the two models discussed above (Abouelleil and Rasheed (2021) and Nayal and Rasheed (2006)) that is shown to correlate well to the test experimental data by Reinhardt (1984). The tension envelope curve utilized in the current formulation is characterized by a multi-linear relationship, on the other hand, the cyclic behavior of the stress-strain relationship is modeled as follows:

Model Calibration:

The current model is based on experimental observations from available data. Based on these observations, the following assumptions are made:

1. The coordinate of the pivot point at which all of the unloading paths intersect if extended linearly is at (-4, -3).
2. The coordinate of the pivot point at which all of the reloading paths intersect if extended linearly is at (-2.8, -1.15).

3. The locus of the inflection points is observed to assume two straight lines defined by the next two items.
4. The first line of inflection points runs between the coordinates of (0, 0.4) and (8.6, 0). Figure 4.7
5. The second line of inflection points runs between the coordinates of (0,0.2) and (30,0). Figure 4.7

- **Envelope Curve:**

Equation (33)-(35) can be used to estimate the envelope curve as follows:

For $0.00 \leq \frac{\varepsilon_e}{\varepsilon_t} \leq 1.00$:

$$y_e = x_e \tag{33}$$

For $1.00 \leq \frac{\varepsilon_e}{\varepsilon_t} \leq 5.64$:

$$y_e = -0.10776\,(x_e) + 1.1077 \tag{34}$$

For $\frac{\varepsilon_e}{\varepsilon_t} < 5.64$:

$$y_e = -0.02052(x_e) + 0.6157 \tag{35}$$

Where the normalized strain (5.64) represents the intersection of the two lines of the hybrid envelope model. See Figure 4.6.

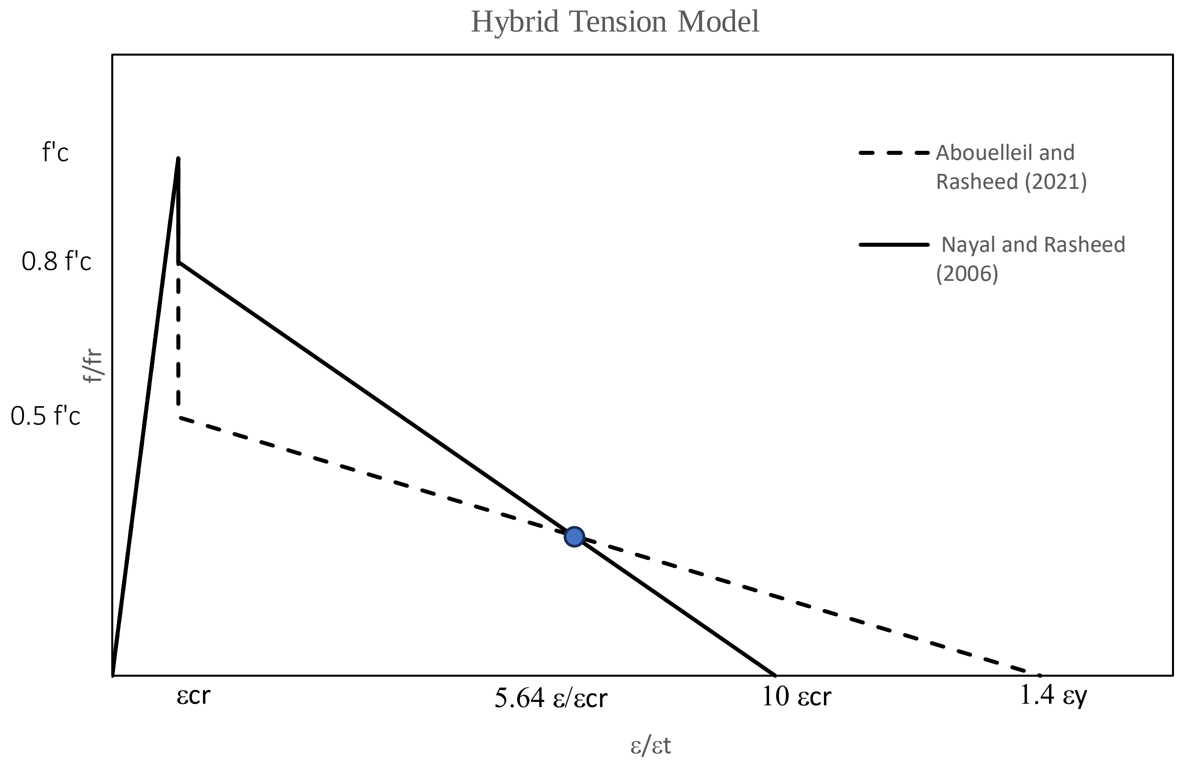

Figure 4.6. Hybrid Concrete Tension Model Derived from the Models Proposed by Abouelleil and Rasheed (2021) and Nayal and Rasheed (2006).

- **Unloading path:**

The slope of any unloading path can be calculated using Equation (36):

$$S_u = \frac{y_e + 3}{x_e + 4} \tag{36}$$

Where:

y_e and x_e are the departure point on the envelope curve.

S_u is the slope of the unloading path.

- **Reloading path:**

The slope of any reloading path can be calculated using Equation (37):

$$S_R = \frac{y_e + 1.15}{x_e + 2.8} \tag{37}$$

Where:

y_e and x_e are the departure point on the envelope curve.

S_R is the slope of the reloading path.

To locate the coordinate of the x intercept of any reloading path, Equation (38) can be used:

$$x_{int} = \frac{-2.8\ S_R + 1.15}{S_R} \tag{38}$$

- **Inflection Points:**

The inflection point can be determined by the intersection of the unloading line and the descending inflection line leading to Equations (39)-(42):

For $0.00 \leq \frac{\varepsilon_e}{\varepsilon_t} \leq 5.02$:

$$x_i = \frac{-4\ S_u + 3.4}{S_u + 0.0465} \tag{39}$$

$$y_i = -0.0465(x_i) + 0.4 \tag{40}$$

For $5.02 < \frac{\varepsilon_e}{\varepsilon_t}$:

$$x_i = \frac{-4\ S_u + 3.2}{S_u + 0.00667} \tag{41}$$

$$y_i = -0.0067(x_i) + 0.2 \tag{42}$$

After developing all the necessary equations, the model was calibrated against the original experimental data to verify its accuracy. The results are presented in Figure 4.8. Further validation was conducted to assess the applicability of the present model in other experiments, as explained in the next section.

Tension Model Verification

Using the calibrated data, this phenomenological model is applied to two other specimens. The predicted hysteric loops are shown in Figure 4.9 and Figure 4.10 in comparison to the actual experimental data. The graphs show a good agreement leading to the conclusion that the developed model effectively represents the behavior of plain concrete under cyclic tension loads.

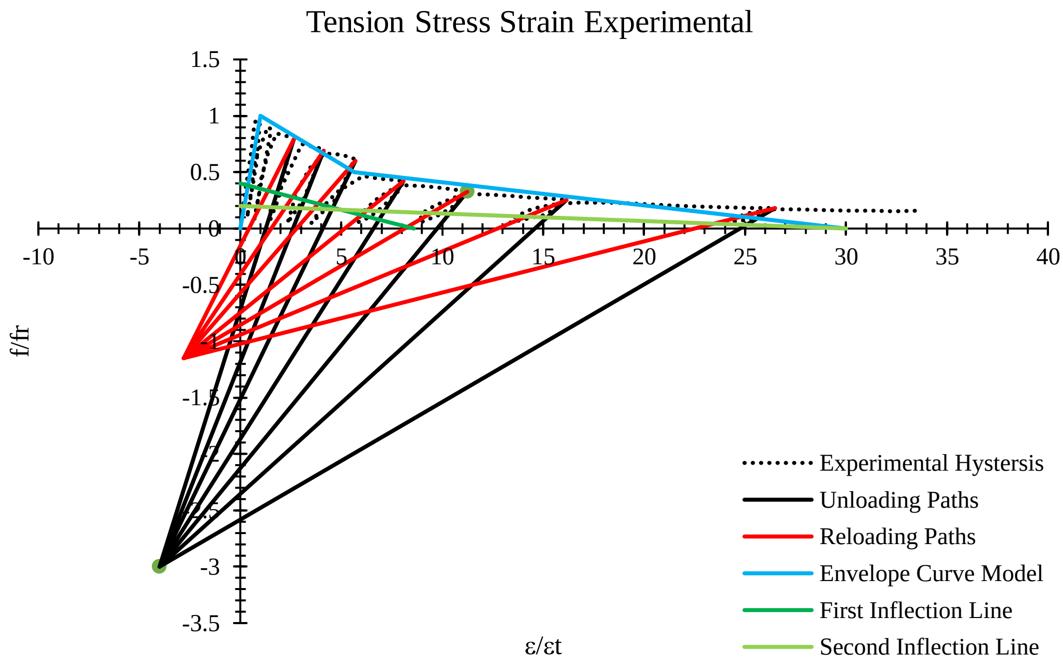

Figure 4.7 Unloading and Reloading Slopes Intersection Points.

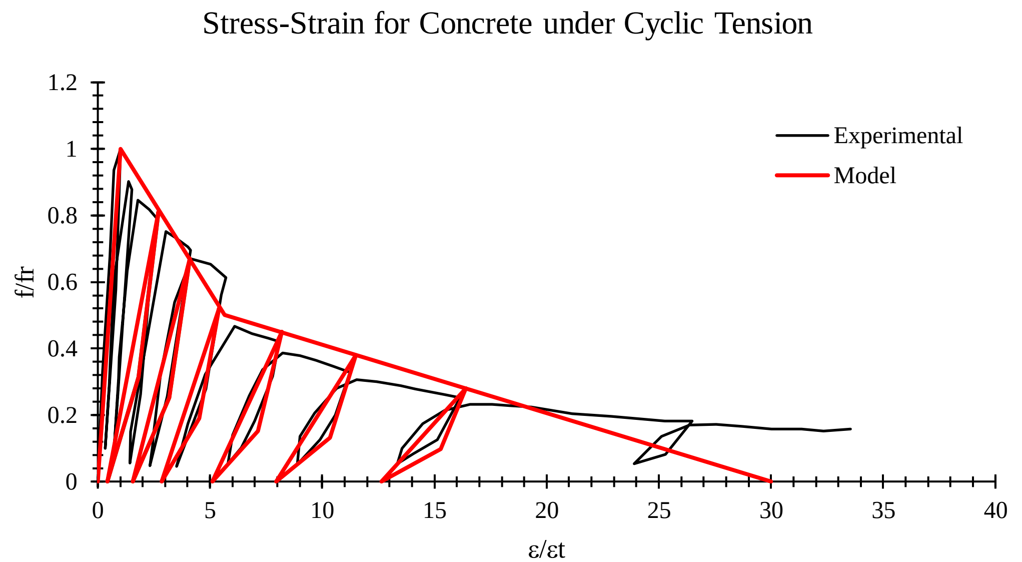

Figure 4.8. Model Calibration from Experimental Data.

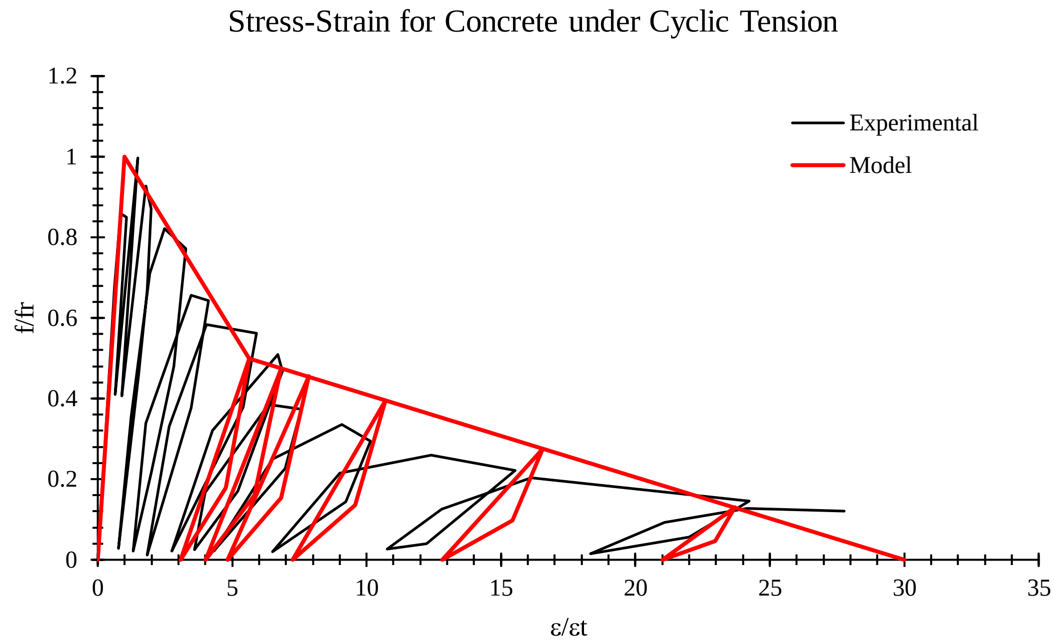

Figure 4.9. Model Verification from Experimental Data No.1.

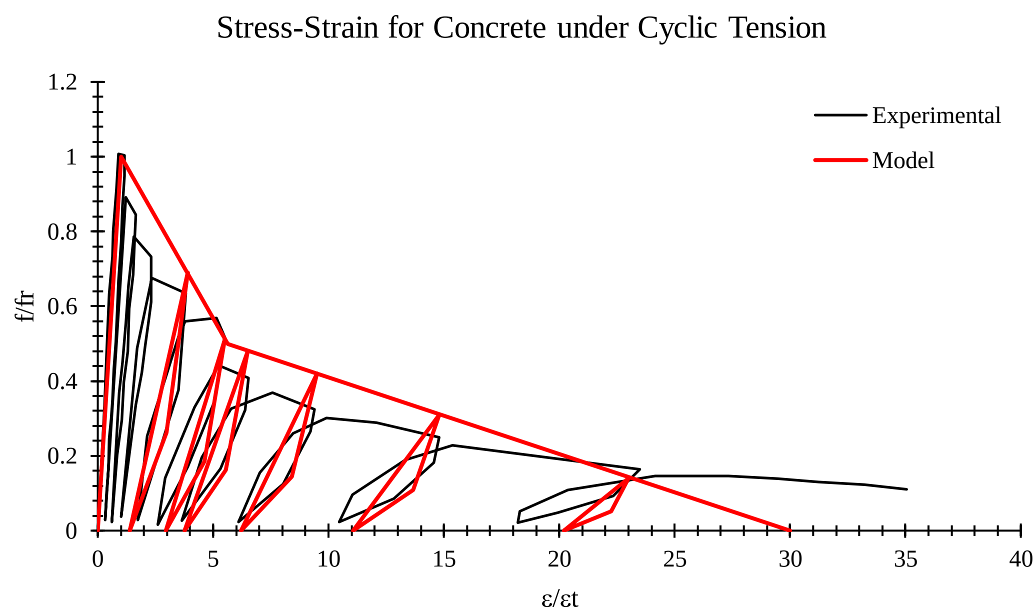

Figure 4.10. Model Verification from Experimental Data No.2.

4-4 Concrete Cyclic Behavior Under Reverse Cyclic Loading:

Since there is a reversed cyclic loading in tension and in compression in the problem to be modeled herein, a review of the experimental results showing reverse cyclic tension and compression was examined. This was found to be different from non-reversed cyclic tension and cyclic compression in the previous two sections. Therefore, the model by Mansour and Hsu (2005) was resorted to in the development of the moment-curvature and load-deflection derivations in Chapter 5.

4-5 Compression Envelope Curve:

The compression envelope curve is identified using the trilinear approach and the proposed phenomenological model as follows:

Model Calibration

- The envelope strain, ε_{ec} , can be found using the trilinear moment-curvature proposed by Rasheed et al. (2013) approach such that:

$$\varepsilon_{\mathrm{cf\,cr}} = \frac{\mathrm{M_{cr}}\,\bar{\mathrm{y}}_{\mathrm{c}}}{\mathrm{E_c}\,\mathrm{I_{gt}}} \tag{43}$$

$$\varepsilon_{\mathrm{cf\,y}} = \frac{\varepsilon_{\mathrm{y}}\mathrm{C_y}}{(\mathrm{d}-\mathrm{C_y})} \tag{44}$$

$$\varepsilon_{\mathrm{ec}} = \varepsilon_{\mathrm{cf\,cr}} + \frac{\mathrm{M_e}-\mathrm{M_{cr}}}{\mathrm{M_y}-\mathrm{M_{cr}}}\left(\varepsilon_{\mathrm{cf\,y}} - \varepsilon_{\mathrm{cf\,cr}}\right) \tag{45}$$

Where:

$\varepsilon_{cf\ cr}$ = The envelope compression strain at cracking.

$\varepsilon_{cf\ y}$ = The envelope compression strain at yielding.

$\bar{y}_c$ = The location of the neutral axis at cracking from the extreme compression fiber found using standard linear elastic transformed section analysis.

C_y = The location of the neutral axis at yielding from the extreme compression fiber found using the trilinear approach.

- A phenomenological model developed from the concrete cyclic compressive loading behavior proposed earlier is presented in Equation (46)-(48) that can be used to estimate the stresses on the envelope curve as shown in Figure 4.11 as follows:

For $0.00 \leq \frac{\varepsilon_c}{\varepsilon'_c} \leq \frac{5.0}{19}$:

$$\frac{\sigma}{f'_c} = 1.71\frac{\varepsilon_c}{\varepsilon'_c} \tag{46}$$

For $\frac{5.0}{19} \leq \frac{\varepsilon_c}{\varepsilon'_c} \leq 1.00$:

$$\frac{\sigma}{f'_c} = 0.0216987 + 1.810073\,\frac{\varepsilon_c}{\varepsilon'_c} - 0.8317718\left(\frac{\varepsilon_c}{\varepsilon'_c}\right)^2 \tag{47}$$

For $1.00 \leq \frac{\varepsilon_c}{\varepsilon'_c} \leq 2.50$:

$$\frac{\sigma}{f'_c} = -0.413\,\frac{\varepsilon_c}{\varepsilon'_c} + 1.413 \tag{48}$$

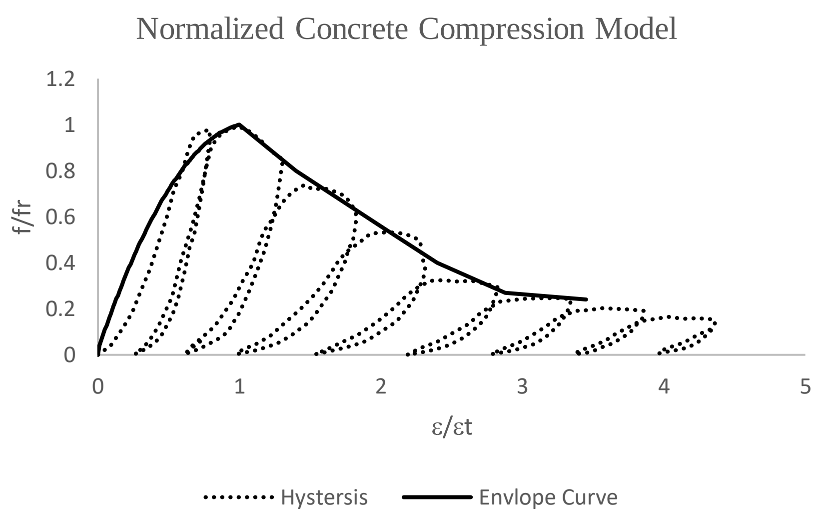

Figure 4.11—Proposed Normalized Compression Model.

4-6 Tension Envelope Curve:

The tension envelope curve is identified using the trilinear approach and the proposed phenomenological model as follows:

Model Calibration:

- The envelope strain, ε_{et} , on the tension envelope curve can also be found using strain compatibility such that:

  $$\varepsilon_{te} = \phi_e \left(h - \frac{\varepsilon_{cf\,e}}{\phi_e}\right) \tag{49}$$

  Where:

  $\varepsilon_{cf\,e}$ = The corresponding envelope compression strain.

- The stress on the tension envelope curve is found using a hybrid model of two models proposed by (Nayal and Rasheed 2006) and (Abouelleil and Rasheed 2021) that is further simplified here as shown in Figure 4.12. The tensile envelope stress is found such that:

  For $(\frac{\varepsilon t_e}{\varepsilon t}) < 1$:

  $$y_e = x_e \tag{50}$$

  For $1 \leq (\frac{\varepsilon t_e}{\varepsilon t}) \leq 5.64$:

  $$y_e = -0.10776\, x_e + 1.1077 \tag{51}$$

  For 5.64 < $(\frac{\varepsilon t_e}{\varepsilon t})$:

  $$y_e = -0.02052(x_e) + 0.615 \tag{52}$$

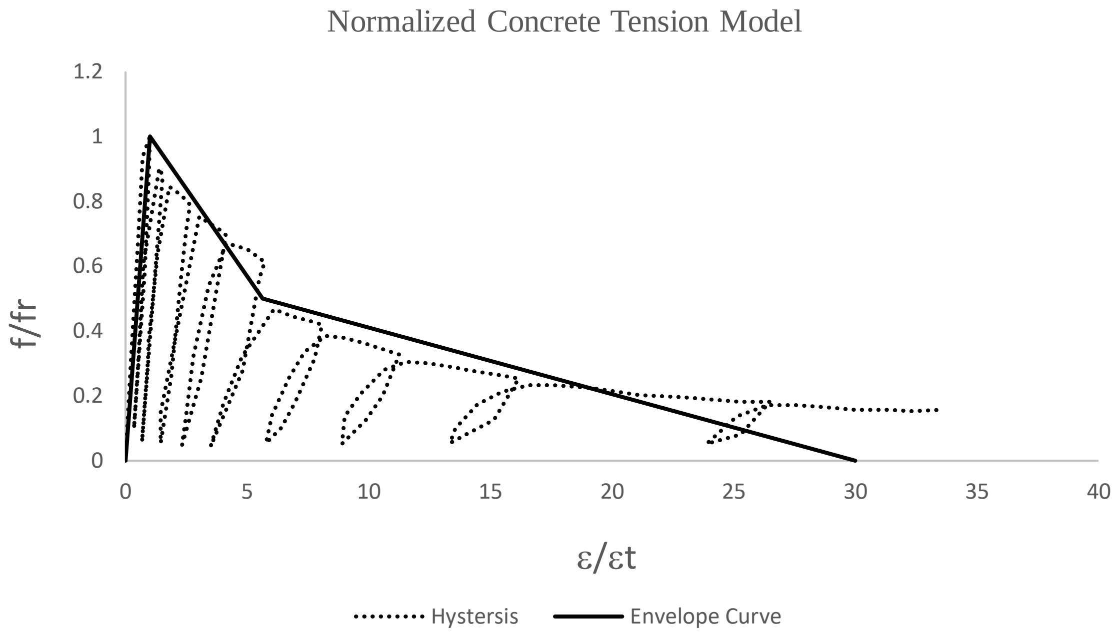

Figure 4.12. Proposed Normalized Tension Model.

4-7 Unloading and Reloading Curves:

The envelope stresses and strains are the principal points from which the inflection point and the residual point on the moment-curvature diagram are derived. The inflection point is a clear feature of the hysteric loop that marks a degradation in stiffness as the loop transitions from the push side to the pull side upon unloading and reloading. While the residual point is the point that marks zero applied load and therefore zero applied moment that accompanies a residual plastic strain.

The following assumptions are made for the derivation of the inflection and residual points:

- When the tensile stress is less than the cracking stress, the response in unloading and reloading is elastic for both the compression and tension side with a slope equal to the initial modulus of concrete E_c.

- After surpassing the cracking stress of concrete at the point of maximum tension f_r and as the load reverses from tension to compression, this reverse action initiates the crack closure phase. The crack closure region is marked by the unloading region on the tension side up to a residual plastic strain point. See Figure 4.1. This region defines the inflection and residual strain, respectively, as:

$$\varepsilon_{ti} = \frac{\varepsilon_{te}}{3} \tag{53}$$

$$\varepsilon_{t\,res} = \frac{\varepsilon_{te}}{5} \tag{54}$$

Where:

ε_{ti} = The inflection strain on the tension side.

$\varepsilon_{t\,res}$ = The residual strain on the tension side.

- Due to the small tensile force change of concrete after cracking during unloading compared to its compressive force change, in most cases, the tensile strain at its inflection and residual state will control the inflection and residual levels at the section unloading response while the compression side remains in the elastic region. Therefore, in the presented work the compression inflection and residual stress-strain levels are identified as follows:

$$\varepsilon_{ci} = r\,\varepsilon_{ec} \tag{55}$$

$$\varepsilon_{c\,res} = 0 \tag{56}$$

Where:

r = The compression stress-strain degradation factor that generates a compression stress-strain corresponding to a tensile stress-strain level marked by inflection.

The model adapted in this chapter proved efficient when employed in Chapter 5 due to its simplicity and accuracy in predicting the key stress-strain values needed to generate the moment-curvature and load deflection responses for any cycle between cracking and yielding loads as will be presented in the next chapter.

4-8 Conclusion:

This chapter proposed a thorough simulation of the behavior of concrete subjected to different cyclic conditions. These conditions are cyclic compression loading, cyclic tension loading and reverse cyclic loading in both tension and compression. The models proposed for the cyclic compression loading and cyclic tension loading take into account the fundamental understanding of concrete damage response that is reflected in the stiffness and strength degradation from the experimental data. The envelope curve for the cyclic compression loading is simulated using a normalized stress-strain values from key points in a linear function followed by a parabolic curve. These points are normalized stresses at zero, and 0.45 (for the linear portion), 0.45 to 1.0 (for the parabolic portion). The post peak region is defined by a linear descending function from 1.0 to 2.5. The experimental test data are used to extract a phenomenological cyclic model, which was characterized by two pivot points at which all the unloading lines and the reloading lines meet. Furthermore, the locus of the inflection points is characterized by descending line that can be used to extract the coordinates of the inflection points for different cycles. The compression cyclic loading model was able to mimic the complex behavior of concrete when verified on two other experimental data.

The same concept is applied for the cyclic tension model. The envelope curve is built as a hybrid model from Nayal and Rasheed (2006) and (Abouelleil and Rasheed (2021) model since it was shown to capture the experimental data closely. The cyclic modeling followed a similar approach to that implemented by the compression model where the unloading lines of different cycles meet at one point and the reloading lines of different cycles meet at another point. The tension cyclic loading model was able to mimic the complex behavior of concrete when verified on two other experimental data.

A thorough examination of experimental results showcasing reversed cyclic tension and compression was conducted as the model proposed is governed by reversed cyclic condition in both tension and compression. This distinct behavior of reversed cyclic loading was observed to deviate from the non-reversed cyclic tension and cyclic compression discussed in the preceding sections. As a result, the model developed by Mansour and Hsu (2005) was adopted for the formulation of moment-curvature and load-deflection relationships presented in Chapter 5.

CHAPTER 5: ANALYTICAL MODEL FOR CYCLIC BEHAVIOR OF RC FRAME MEMBERS STRENGTHENED WITH SECURED CFRP SHEETS USING FIBER ANCHORS

5-1 Introduction:

This is a first attempt introducing a fully analytical model for the hysteresis cycles, unlike the model in Chapter 3 that is purely phenomenological. In this treatment, there are a few observations and assumptions that guide the analytical formulation, which will make it easier to avoid a full fledge numerical solution on the stress-strain level.

5-2 Moment-Curvature Response of Hysteretic Cycles:

The proposed model employs sectional analysis to predict the unloading portion of the moment-curvature response of the column. An analysis approach, similar in concept to the one used to develop the idealized trilinear moment-curvature model, is devised here. For that purpose, the trilinear moment-curvature model is heavily used to obtain the envelope values for the vertical frame member, and it is then further analyzed to plot two other distinct points on the unloading portion of any hysteresis loop. These points are the envelope moment-curvature point, Me-ϕe, the inflection moment-curvature point on the unloading side, Mi-ϕi, and the residual moment-curvature point on the unloading side, M_{res}-ϕ_{res}, that strongly define the moment-curvature response for FRP-strengthened vertical frame members under cyclic loading.

The moment-curvature model is based on the following assumptions:

1. Upon unloading, there is an inflection point in the M-ϕ cycles that takes place at a tensile unloading degradation inflection point beyond cracking corresponding to a certain level of

elastic unloading on the compression side, $\varepsilon_{\mathrm{ci}} = (1-\mathrm{r})\varepsilon_{\mathrm{ce}}$, $\Delta\varepsilon_{\mathrm{c\,e-i}} = \mathrm{r}\,\varepsilon_{\mathrm{ce}}$ where r is a fraction of 1.See Figure 5.1.

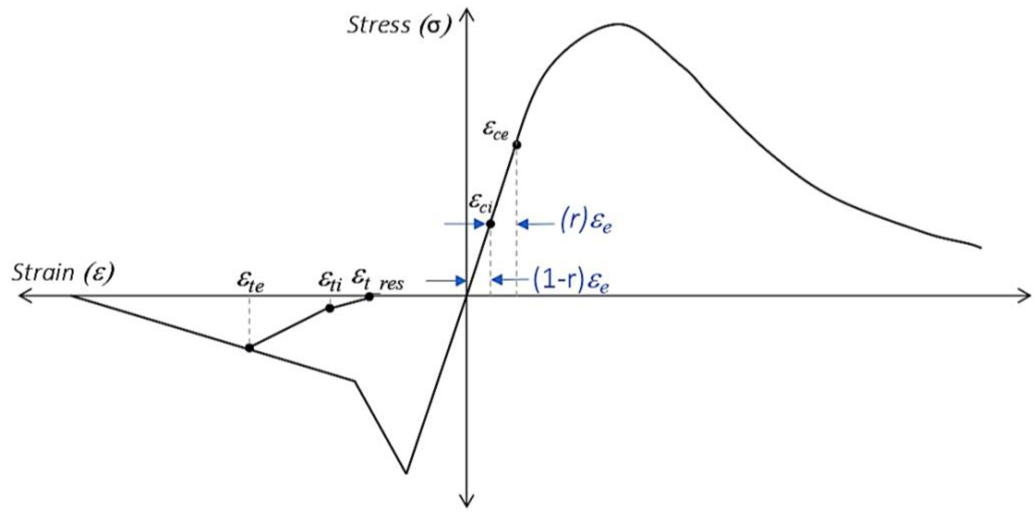

Figure 5.1.Tension Stresses and Strains at Inflection and Residual Points with The Corresponding Points in Compression.

2. The degradation of tensile strain will drop from $\varepsilon_{\mathrm{te}}$ at the envelope curve to $\varepsilon_{\mathrm{te}}/3$ at inflection as shown by Mansour and Hsu (2005) and verified here by comparing to the experimental data.
3. To obtain the compression stress corresponding to the compressive strain in point 1 above, the compressive strain is multiplied by E_{c} to yield ($\Delta\sigma_{(e-i)} = r\,E_c\varepsilon_{ce}$, $\sigma_i = (1-r)\,E_c\,\varepsilon_{ce}$), where r is an unknown to be computed from the force equilibrium equation.
4. To obtain the tensile stress corresponding to the tensile strain in point 2 above, there will be a need to define rules for degradation models. However, since the unloading happens after cracking, the stress contribution of the tensile zone can be neglected.

5. Steel in compression and tension are also in the elastic range since the loops analyzed herein are all before steel yielding. The curvature value ϕ_i and the corresponding neutral axis depth c_i can be defined in terms of $\varepsilon_{\text{ci}} = (1 - \text{r})\varepsilon_{\text{ce}}$, $\varepsilon_{\text{ti}} = \frac{\varepsilon_{\text{te}}}{3}$. See Figure 5.2.

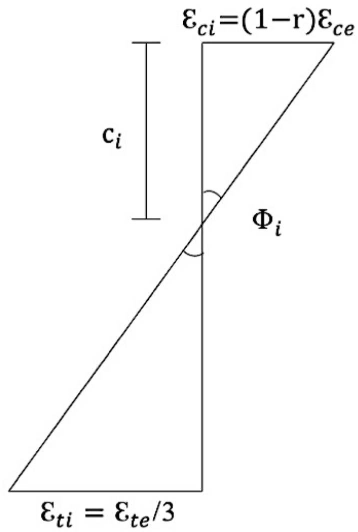

Figure 5.2 Inflection Strain Diagram in Tension and Compression.

6. Invoking equilibrium of forces $\sum f_x = 0$ of the section at the inflection point, the unknown ratio (r) is recovered as follows:

$$\sum f_x = 0 = (1-r)\,\varepsilon_{ce}\,E_c\left(\frac{b\,C_i}{2}\right) + \phi_i\,(c_i - d')\,E_s A_s + E_f\,(1-r)\,\varepsilon_{ce}\,A_f -$$

$$\phi_i\,(d - c_i)\,E_s A_s - E_f\,\frac{\varepsilon_{te}}{3}\,A_f \qquad (57)$$

Where:

$$\phi_i = \frac{(1-r)\,\varepsilon_{ce} + \frac{\varepsilon_{te}}{3}}{h} \qquad (58)$$

$$ci = \frac{(1-r)\,\varepsilon_{ce}}{\phi_i} \qquad (59)$$

7. Once r is evaluated, the value of the inflection moment (M_i) is written in terms of the moments produced by concrete in compression, steel in compression and tension, and

CFRP in compression and tension while ignoring the small concrete contribution in tensions after cracking:

$$M_{i-res} = (1-r)\varepsilon_{ce}E_c\left(\frac{b\,c_i}{2}\right)\left(\frac{h}{2} - \frac{c_i}{3}\right) + \phi_i\,(c_i - d')\,E_sA_s\left(\frac{h}{2} - d'\right) + E_f\,(1 - r)\,\varepsilon_{ce}\,A_f\,\left(\frac{h}{2}\right) + \phi_i\,(d - c_i)\,E_sA_s\left(\frac{h}{2} - d'\right) + E_f\,\frac{\varepsilon_{te}}{3}\,A_f\left(\frac{h}{2}\right) \qquad (60)$$

8. Upon further unloading beyond the inflection point (M_i, ϕ_i) in the M-ϕ cycle, a residual point (0, ϕres) exists when the tensile extreme fiber degrading strain crosses the x-axis postulated at ($\varepsilon_{te}/5$), while the compressive extreme fiber strain unloads to the origin at zero strain-zero stress. See Figure 5.3.

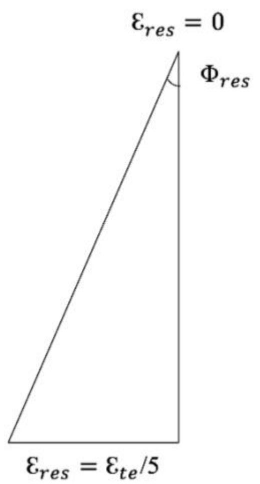

Figure 5.3. Residual Strain Diagram in Tension and Compression.

9. Once the residual point is reached, the loop is assumed to unload linearly to the envelope point on the other side of cycle response.

10. The reloading path follows a mirror image of the unloading path in reverse side about the origin.

5-3 Model Verification

The graphs shown in Figure 5.4 to Figure 5.11 are the attempts of model prediction plotted against experimental data. It is noteworthy to mention that four curvature data cycles are presented for the experimental results as each one of them is calculated using two out of the four strain gauge values across the geometric centroid. Curvature one is obtained using the North-West/North-East strain gauges, curvature two is obtained using the South-West/South-East strain gauges, curvature three is obtained using the North-East/South-West strain gauges, and curvature four is obtained using the North-West/South-East strain gauges.

BCA-4:

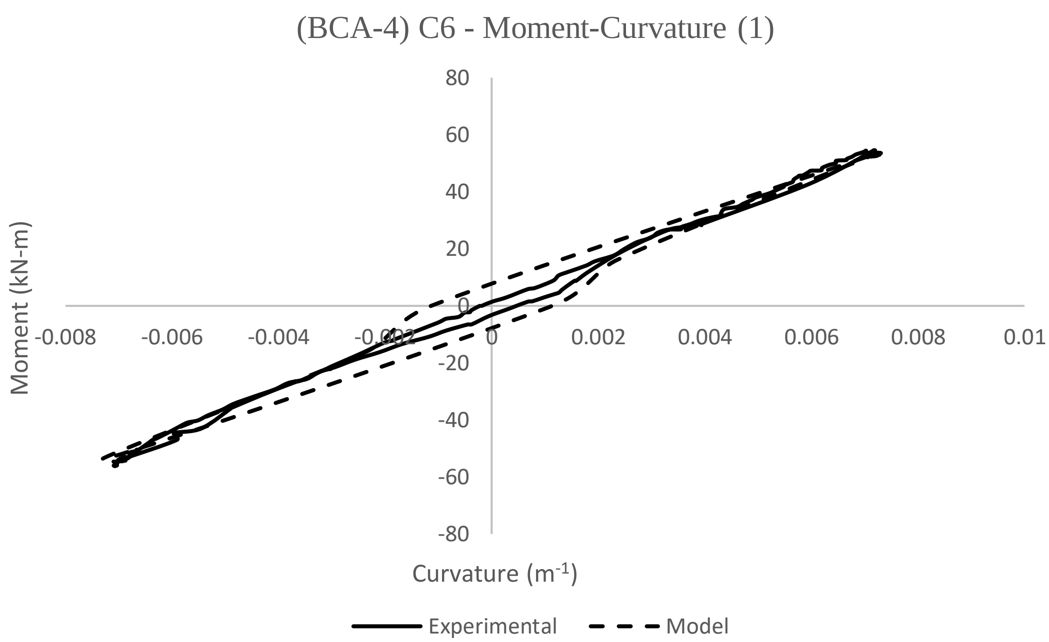

Figure 5.4. Model Prediction of Moment-curvature (1) for BCA-4.

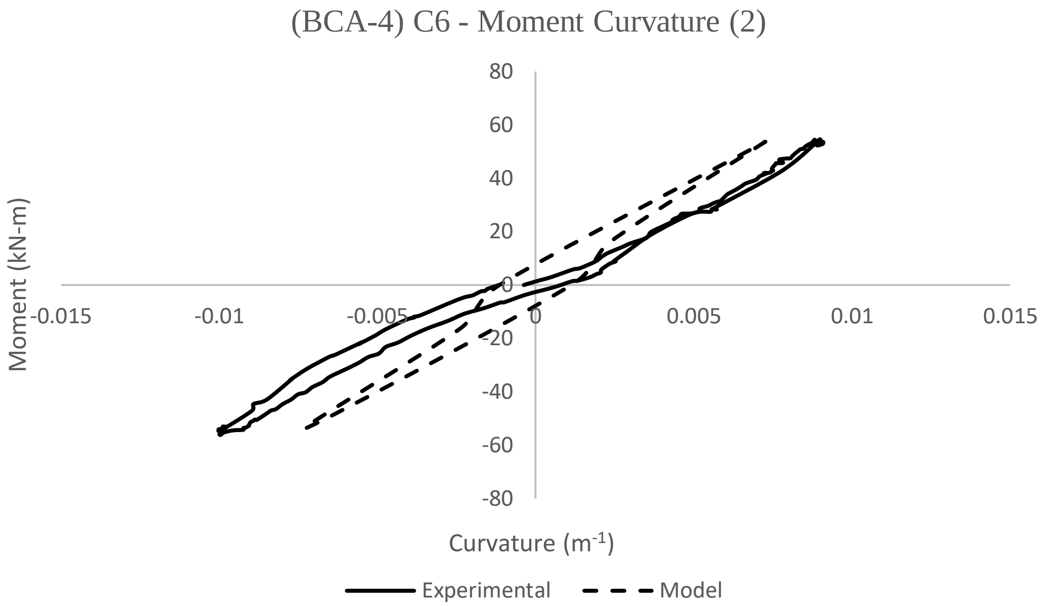

Figure 5.5. Model Prediction of Moment-curvature (2) for BCA-4.

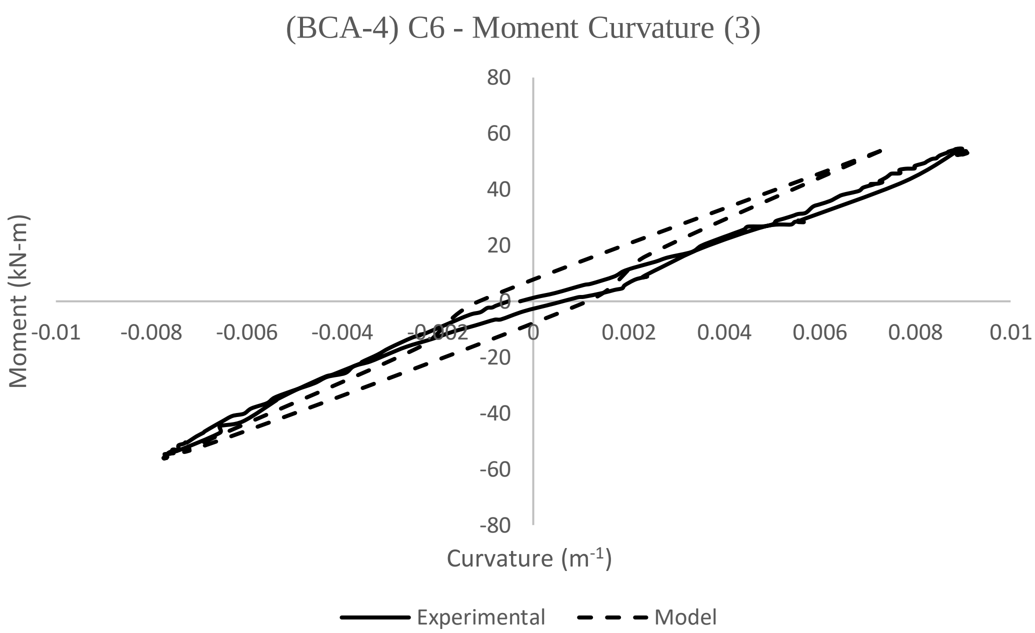

Figure 5.6. Model Prediction of Moment-curvature (3) for BCA-4.

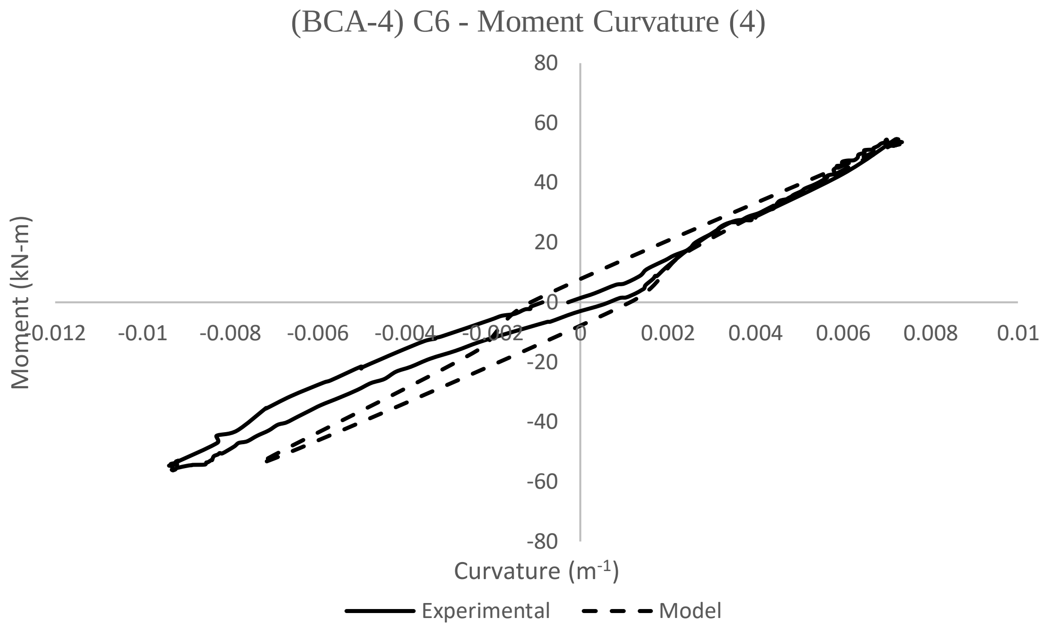

Figure 5.7. Model Prediction of Moment-curvature (4) for BCA-4.

BCA-5:

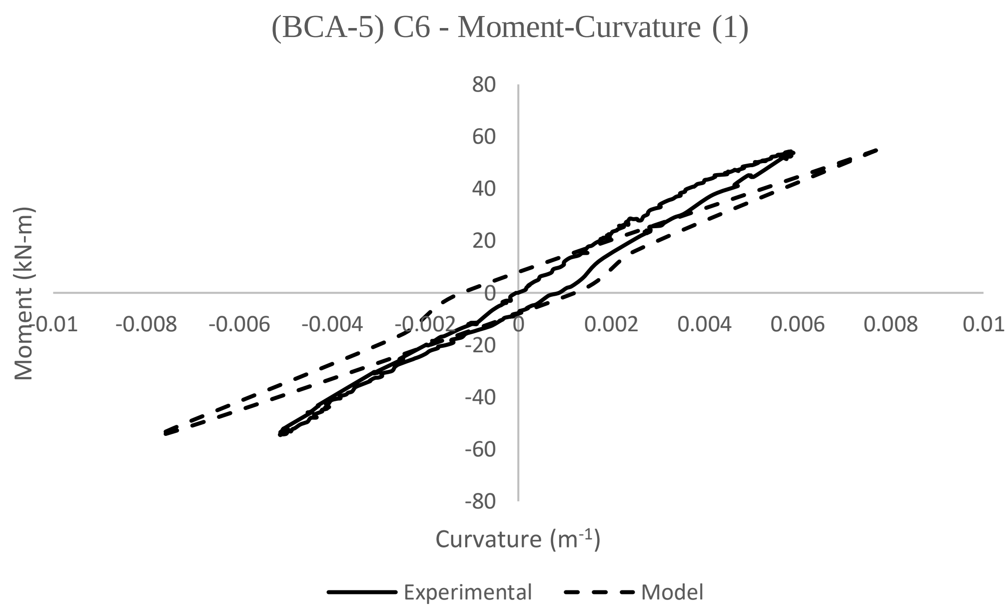

Figure 5.8. Model Prediction of Moment-curvature (1) for BCA-5.

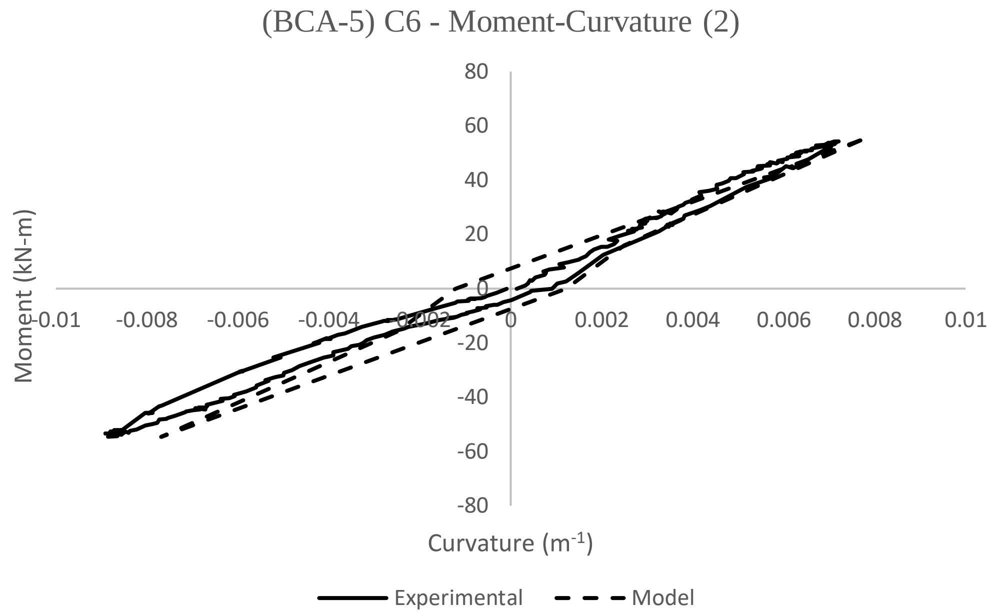

Figure 5.9. Model prediction of Moment-curvature (2) for BCA-5.

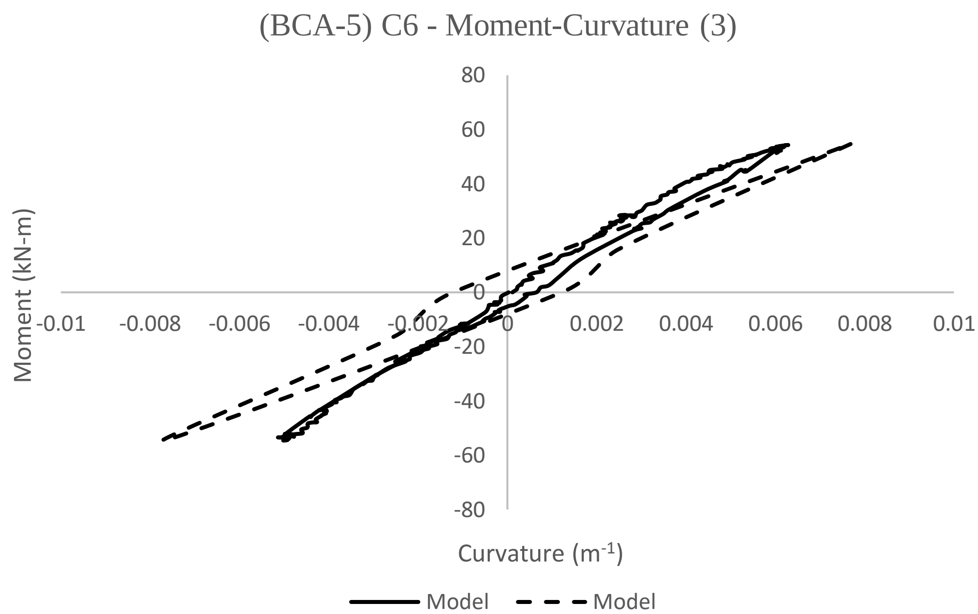

Figure 5.10. Model Prediction of Moment-curvature (3) for BCA-5.

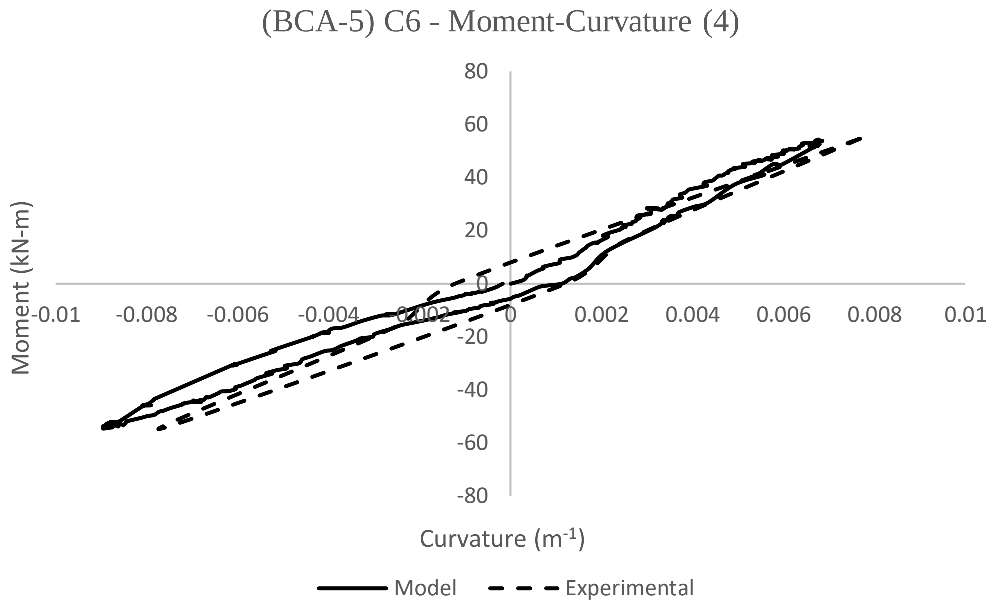

Figure 5.11.Model Prediction of Moment-curvature (4) for BCA-5.

5-4 Load-Deflection Response for a Hysteretic Cycle:

Similar to the analytical formulation based on the trilinear moment-curvature curve for the monotonic envelope curve, this work is intended to derive closed form analytical load-deflection expressions for the unloading portion of any hysteresis loop under consideration. However, the present equations are adapted to cycles prior to yielding simply because the experimental cycles are fully depicted and available in that range of loading.

The following assumptions are adopted in this work:

1. The inflection points (M_i, ϕ_i) are determined from the moment-curvature treatment presented in section 5.2 above.
2. The inflection point along the uncracked envelope line (M_{cri}, ϕ_{cri}) is derived from the structural system as follows:

$$\mathrm{Me} = \mathrm{Pe\,La} \rightarrow \mathrm{Pe} = \frac{\mathrm{Me}}{\mathrm{La}}$$

$$\mathrm{Mcr} = \mathrm{Pe\,Lu} \rightarrow \mathrm{Pe} = \frac{\mathrm{Mcr}}{\mathrm{Lu}}$$

$$\mathrm{Mi} = \mathrm{Pi\,La} \rightarrow \mathrm{Pi} = \frac{\mathrm{Mi}}{\mathrm{La}}$$

$$\mathrm{Mcri} = \mathrm{Pi\,Lu} \rightarrow \phi_{cri} = \frac{\mathrm{Mcri}}{E_c I_{gt}}$$

3. Connecting the two points (M_i, ϕ_i) and (M_{cri}, ϕ_{cri}) with a straight line as shown in Figure 5.12, the Mi(x) and ϕ_i (x) at any distance x measured from the applied load as shown in Figure 5.13 is defined as:

$$\mathrm{Mi(x)} = \mathrm{Pi\,x} \quad (61)$$

$$\phi_i(x) = \phi_{cri} + \frac{M_i(x) - M_{cri}}{M_i - M_{cri}} (\phi_i - \phi_{cri}) \quad (62)$$

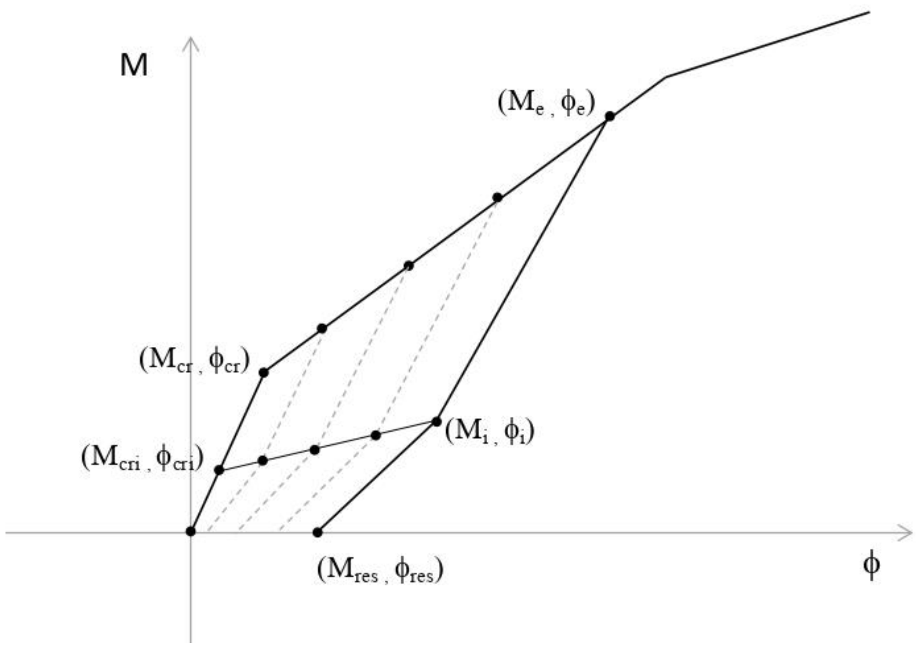

Figure 5.12. The Various Inflection Points Along the Inflection Line on The Moment-Curvature Diagram During Unloading.

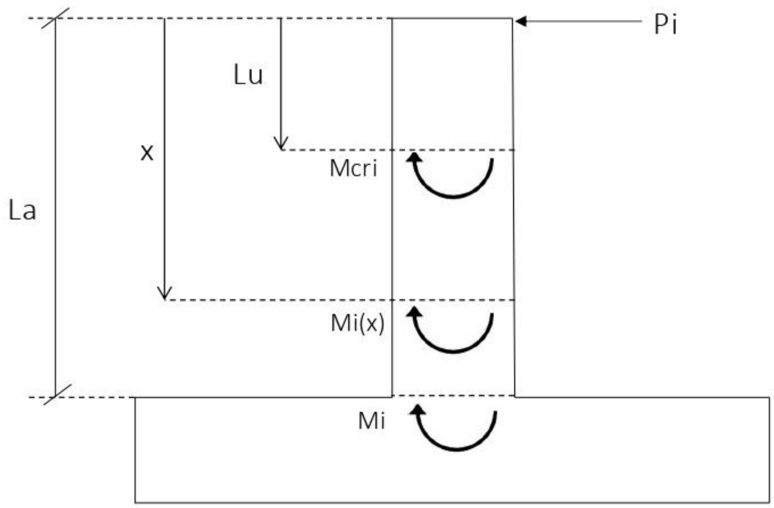

Figure 5.13. The Various Moment-curvature Regions Generalized for the RC Frame.

4. By substituting the moment area expression, the change in deflection and rotation between the envelope point and the inflection point are integrated from:

$$\delta\Delta_{(e-i)} = \int_0^{Lu} x\,(\phi_e(x) - \phi_i(x))\,dx + \int_{Lu}^{La} x\,(\phi_e(x) - \phi_i(x))\,dx$$

$$\delta\theta_{B(e-i)} = \int_0^{LuB} \frac{x}{L_B}\left(\emptyset_{e_B}(x) - \emptyset_{i_B}(x)\right)dx + \int_{LuB}^{LB} \frac{x}{L_B}\left(\emptyset_{e_B}(x) - \emptyset_{i_B}(x)\right)dx$$

The above integrations are performed analytically in the formulation section below to extract the deflection and rotation expressions.

5. Similarly, the moment at the residual point ($M_{res} = 0$). The curvature at the residual point is obtained from the moment-curvature treatment in section 5.2.

6. The $\phi_{cr\_res} = 0$ and the ϕ_{res} (x) may be determined from by a linear function between zero and ϕ_{res} .

$$\phi_{res}(x) = 0 + \frac{M_i(x) - M_{cri}}{M_i - M_{cri}} (\phi_{res} - 0) \quad (63)$$

7. By substituting the moment area expression, the change in deflection and rotation between the inflection point and the residual point are integrated from:

$$\delta\Delta_{i-res} = \int_0^{Lu} x\,(\phi_i(x) - \phi_{res}(x))\,dx + \int_{Lu}^{La} x\,(\phi_i(x) - \phi_{res}(x))\,dx$$

$$\delta\theta_{B(i-res)} = \int_0^{LuB} \frac{x}{L_B}\left(\emptyset_{i_B}(x) - \emptyset_{res_B}(x)\right) dx + \int_{LuB}^{LB} \frac{x}{L_B}\left(\emptyset_{i_B}(x) - \emptyset_{res_B}(x)\right) dx$$

8. Once the load-deflection points at inflection and residual location are drawn linearly from the envelope point. Then the residual point is connected directly to the envelope point on the pull side.
9. By mirroring the unloading path about the origin in reverse order for reloading path, the full cycle is constructed. In other words, the reloading path goes from envelope on the pull side to inflection on the pull side to the residual on the pull side then back to the envelope point on the push side, Figure 5.14.

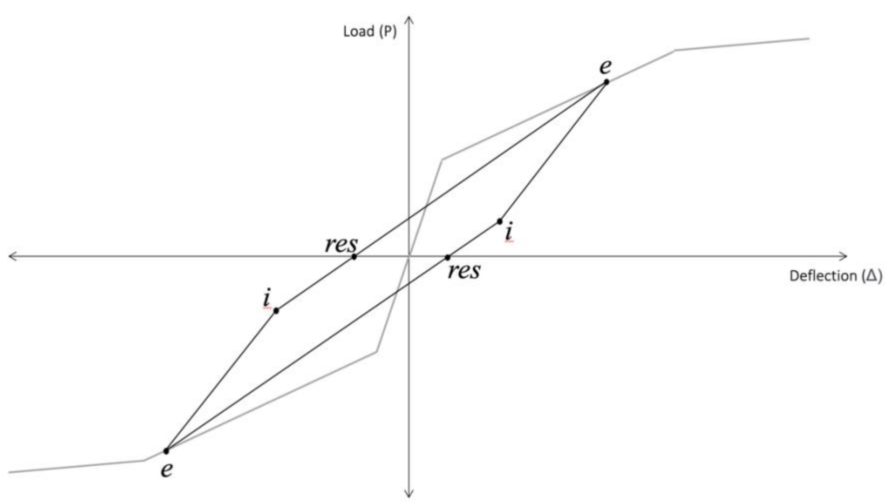

Figure 5.14. The Predicted Load Deflection Envelope, Inflection, And Residual Points on The Push and Pull Side.

The above integrations are performed analytically in the formulation section below to extract the deflection and rotation expressions.

Formulation

The column tip deflection in a vertical frame member is obtained by the analytical integration of the curvature along the length of the column in addition to the contribution of the beam as presented below:

$$\delta\Delta_{\mathrm{tip}_{(e-i)}} = \delta\Delta_{e-i} + \delta\theta_{B_{(e-i)}}(L_c) \tag{64}$$

Where:

$$\delta\Delta_{e-i} = \delta\Delta_{e-i_1} + \delta\Delta_{e-i_2} \tag{65}$$

Where $\delta\Delta_{e-i_1}$ is the deflection change from zero moment to cracking moment, such that:

$$\delta\Delta_{e-i_1} = \int_0^{Lu} x\big(\emptyset_e(x) - \emptyset_i(x)\big)dx = \int_0^{Lu} \frac{M_e(x)}{E_c I_{gt}} - \frac{M_i(x)}{E_c I_{gt}} dx = \int_0^{Lu} x \frac{P_e x}{E_c I_{gt}} - \frac{P_i x}{E_c I_{gt}} dx$$

The solution of the integration is:

$$\delta\Delta_{e-i_1} = \frac{(P_e - P_i)L_u^3}{3\,E_c I_{gt}} \tag{66}$$

Where:

$$L_u = \frac{M_{cr}}{P_e}$$

$\delta\Delta_{e-i_2}$ is the deflection change from cracking moment to maximum moment, such that:

$$\delta\Delta_{e-i_2} = \int_{Lu}^{La} \left(\emptyset_{cre}(x) - \emptyset_{cri}(x)\right) x\,dx + \int_{Lu}^{La} \left(\frac{-M_{cre}(x)}{\text{Slope 2 e}} + \frac{M_{cri}(x)}{\text{Slope 2 i}}\right) x\,dx$$

$$+ \int_{Lu}^{La} \left(\frac{M_e}{\text{Slope 2e}} - \frac{M_i}{\text{Slope 2 i}}\right) x\,dx$$

The solution of the integration is:

$$\delta\Delta_{e-i_2} = (\emptyset_{cre} - \emptyset_{cri})\left(\frac{(L_a^2 - L_u^2)}{2}\right) - \left(\frac{M_{cre}}{\text{Slope 2 e}} - \frac{M_{cri}}{\text{Slope 2 i}}\right)\left(\frac{(L_a^2 - L_u^2)}{2}\right) + \left(\frac{P_e}{\text{Slope 2 e}} - \frac{P_i}{\text{Slope 2 i}}\right)\left(\frac{(L_a^3 - L_u^3)}{3}\right) \tag{67}$$

Therefore:

$$\boldsymbol{\delta\Delta_{e-i}} = \left(\frac{(P_e - P_i)L_u^3}{3\,E_c I_{gt}}\right) + \left((\emptyset_{cre} - \emptyset_{cri})\left(\frac{(L_a^2 - L_u^2)}{2}\right)\right) - \left(\left(\frac{M_{cre}}{\text{Slope 2 e}} - \frac{M_{cri}}{\text{Slope 2 i}}\right)\left(\frac{(L_a^2 - L_u^2)}{2}\right)\right) + \left(\left(\frac{P_e}{\text{Slope 2 e}} - \frac{P_i}{\text{Slope 2 i}}\right)\left(\frac{(L_a^3 - L_u^3)}{3}\right)\right) \tag{68}$$

Where:

P_i = the load corresponding to the inflection point load level.

L_u= The span length corresponding to uncracked region

E_c= Concrete young's modulus.

I_{gt}= transformed gross moment of inertia

$\emptyset_{cri}$= Curvature corresponding to the inflection curvature reflected on the uncracked envelope moment-curvature segment, See Figure 5.12

M_{cri}= Moment corresponding to the inflection moment reflected on the uncracked envelope moment-curvature segment, See Figure 5.12

$Slope_{2i}$= The slope of the line from cracking inflection point to the maximum inflection point on a moment-curvature hysteresis loops, See Figure 5.12

$Slope_{2e}$= The slope of the line from cracking envelope point to the yielding envelope point on a moment-curvature envelope curve.

Beam contribution $\delta\theta_{B_{(e-i)}}(L_c)$ can be found as follows:

$$\delta\theta_{B_{(e-i)}} = \delta\theta_{B_1} + \delta\theta_{B_2}$$

$$\delta\theta_{B_1} = \int_0^{LuB} \frac{x}{L_B}\left(\emptyset_{e_B}(x) - \emptyset_{i_B}(x)\right) dx = \int_0^{LuB} \frac{x}{L_B}\left(\frac{M_{e_B}(x)}{E_c I_{gt}} - \frac{M_{i_B}(x)}{E_c I_{gt}}\right) dx$$

$$= \int_0^{LuB} \frac{x}{L_B}\left(\frac{P_e x}{E_c I_{gt}} - \frac{P_i x}{E_c I_{gt}}\right) dx$$

The solution of the integration is:

$$\delta\theta_{B_1} = \frac{(P_{Be} - P_{Bi}) L_{uB}^3}{3\, E_c I_{gt}\, L_B} \quad (69)$$

Where:

$$P_{Be} = \frac{M_{Be}}{L_B} = \frac{M_e}{2L_B} \quad (70)$$

$$P_{Bi} = \frac{M_{Bi}}{L_B} = \frac{M_i}{2L_B} \quad (71)$$

$$L_{uB} = \frac{M_{cre}}{P_{Be}} \quad (72)$$

$$M_{cri} = P_{Bi} L_{uB} \quad (73)$$

$$\delta\theta_{B_2} = \int_{LuB}^{LB} (\emptyset_{cre} - \emptyset_{cri}) \frac{x}{L_B} dx + \int_{LuB}^{LB} \left(\frac{-M_{cre}}{\text{Slope 2 e}} + \frac{M_{cri}}{\text{Slope 2 i}}\right) \frac{x}{L_B} dx$$

$$+ \int_{Lu}^{La} \left(\frac{P_e}{\text{Slope 2e}} - \frac{P_i}{\text{Slope 2 i}}\right) \frac{x^2}{L_B} dx$$

The solution of the integration is:

$$\delta\theta_{B_2} = (\emptyset_{cre} - \emptyset_{cri}) \left(\frac{(L_B^2 - L_{uB}^2)}{2L_B}\right) - \left(\frac{M_{cre}}{\text{Slope 2 e}} - \frac{M_{cri}}{\text{Slope 2 i}}\right) \left(\frac{(L_B^2 - L_{uB}^2)}{2L_B}\right) + \left(\frac{P_{Be}}{\text{Slope 2 e}} - \frac{P_{Bi}}{\text{Slope 2 i}}\right) \left(\frac{(L_B^3 - L_{uB}^3)}{3L_B}\right) \quad (74)$$

$$\delta\theta_{B_{(e-i)}} = \frac{(P_{Be} - P_{Bi}) L_{uB}^3}{3\, E_c I_{gt}\, L_B} + (\emptyset_{cre} - \emptyset_{cri}) \left(\frac{(L_B^2 - L_{uB}^2)}{2L_B}\right) - \left(\frac{M_{cre}}{\text{Slope 2 e}} - \frac{M_{cri}}{\text{Slope 2 i}}\right) \left(\frac{(L_B^2 - L_{uB}^2)}{2L_B}\right) + \left(\frac{P_{Be}}{\text{Slope 2 e}} - \frac{P_{Bi}}{\text{Slope 2 i}}\right) \left(\frac{(L_B^3 - L_{uB}^3)}{3L_B}\right) \quad (75)$$

Where, If $L_{uB} > L_B$, then $\delta\theta_{B_2}$ is zero.

The residual deflection can be found from the change in deflection between the inflection point to the residual point at which the applied load is zero.

$$\delta\Delta_{tip_{(i-res)}} = \delta\Delta_{i-res} + \delta\theta_{B_{(i-res)}}(L_c) \quad (76)$$

$$\delta\Delta_{i-res} = \delta\Delta_{i-res_1} + \delta\Delta_{i-res_2} = \int_0^{Lu} x(\emptyset_{cri}(x))\, dx + \int_{Lu}^{La} x(\emptyset_i(x) - \emptyset_{res}(x))\, dx$$

The solution of the integration and simplification of terms yield:

$$\delta\Delta_{i-res} = \emptyset_{cri} \frac{L_a^2}{2} + P_i \frac{L_a^3 - L_u^3}{3} \left(\frac{1}{\text{Slope}_{2i}} - \frac{1}{\text{Slope}_{res}}\right) - M_{cri} \frac{L_a^2 - L_u^2}{2} \left(\frac{1}{\text{Slope}_{2i}} - \frac{1}{\text{Slope}_{res}}\right) \quad (77)$$

$$\delta\theta_{B_{(i-res)}} = \int_0^{LuB} \frac{x}{L_B} (\emptyset_{cri}(x)) dx + \int_{LuB}^{LB} \frac{x}{L_B} (\emptyset_{Bi}(x) - \emptyset_{B\,res}(x)) dx$$

The solution of the integration and simplification of terms yield:

$$\delta\theta_{B_{(i-res)}} = \emptyset_{cri}\frac{L_B^2}{2} + P_i\frac{L_B^3 - L_{uB}^3}{6L_B}\left(\frac{1}{Slope_{2i}} - \frac{1}{Slope_{res}}\right) - M_{cri}\frac{L_B^2 - L_{uB}^2}{2L_B}\left(\frac{1}{Slope_{2i}} - \frac{1}{Slope_{res}}\right) \quad (78)$$

Therefore:

$$\delta\Delta_{tip_{(i-res)}} = \left(\emptyset_{cri}\frac{L_a^2}{2} + P_i\frac{L_a^3 - L_u^3}{3}\left(\frac{1}{Slope_{2i}} - \frac{1}{Slope_{res}}\right) - M_{cri}\frac{L_a^2 - L_u^2}{2}\left(\frac{1}{Slope_{2i}} - \frac{1}{Slope_{res}}\right)\right) +$$

$$(L_C)\left(\emptyset_{cri}\frac{L_B^2}{2} + P_i\frac{L_B^3 - L_{uB}^3}{6L_B}\left(\frac{1}{Slope_{2i}} - \frac{1}{Slope_{res}}\right) - M_{cri}\frac{L_B^2 - L_{uB}^2}{2L_B}\left(\frac{1}{Slope_{2i}} - \frac{1}{Slope_{res}}\right)\right) \quad (79)$$

5-5 Model Verification

The procedure and equations presented in section 5.4 are used to predict the sixth cycle of the load-deflection hysteretic loop for specimens BCA-4 and BCA-5 in Figure 5.15 and Figure 5.16, respectively.

BCA-4:

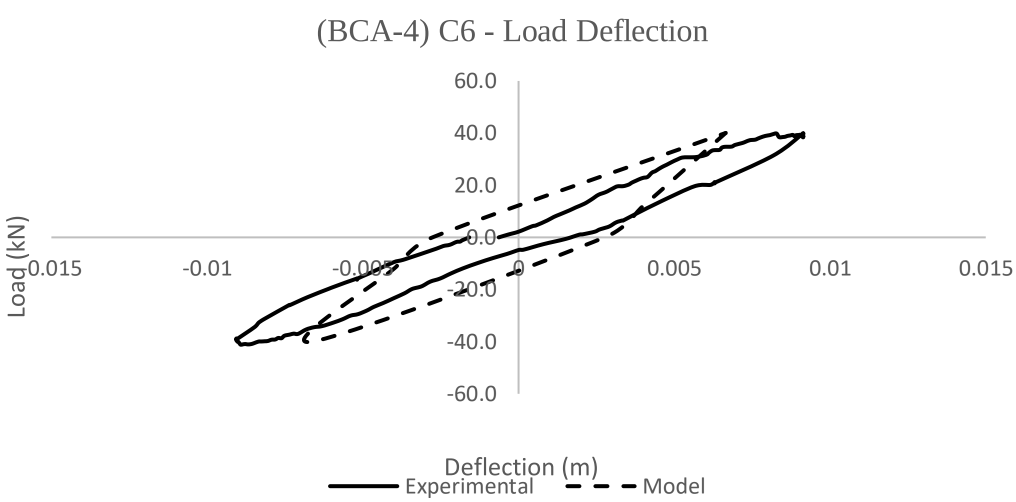

Figure 5.15. Experimental vs. Predicted Model Load-deflection Loop for Load Cycle 6 (C6) for Specimen BCA-4.

BCA-5:

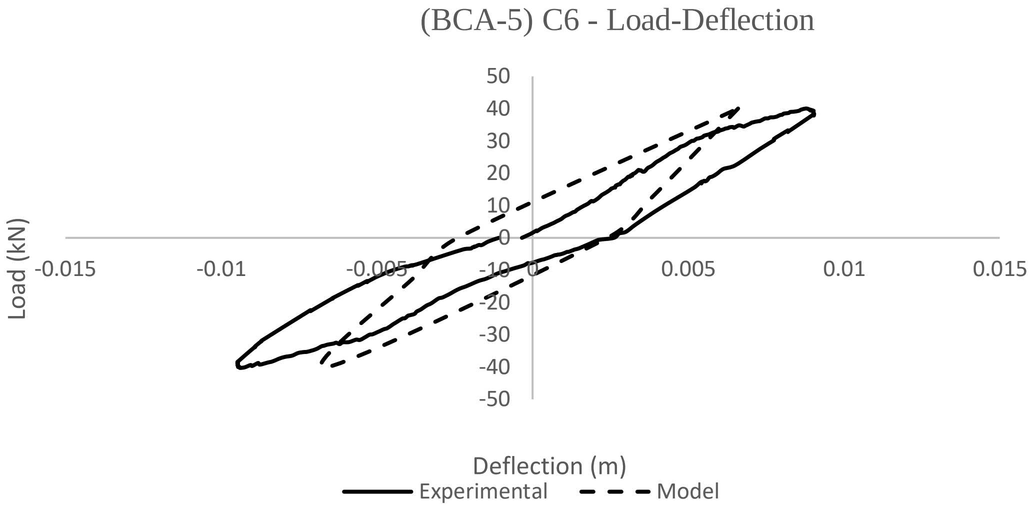

Figure 5.16. Experimental vs. Predicted Model Load-Deflection Loop for Load Cycle 6 (C6) for Specimen BCA-5.

5-6 Conclusion:

In this study, a first attempt to derive an analytical model is presented to predict the moment-curvature and load-deflection responses of a CFRP-strengthened RC vertical frame member under cyclic loading. This model is fundamentally based on the trilinear moment-curvature approach, developed by Charkas et al. (2003) for monotonic loading and a comprehensive concrete cyclic tension-compression behavior model that is merged work of the analytical model presented by (Mansour and Hsu 2005), (Abouelleil and Rasheed 2021), as well as a phenomenological observation that is adopted in this work based on experimental data findings at the residual curvature point. In this work, the trilinear model is extended on the push and pull side to determine the full envelope response of the vertical frame member at any hysteretic loop between cracking and yielding moments. It is also used to express the curvature distribution along the length of the beam-column assembly that is integrated analytically for closed form column tip deflection expressions.

To validate the effectiveness of this novel analytical model, it is used to predict the behavior of two specimens. The model not only showed a good agreement to the overall hysteretic behavior of the frame assembly but reflected an excellent prediction for the location of the inflection and residual moment-curvature points against the experimental data used. Overall, this model presents an excellent first attempt for cyclic analytical moment-curvature and load-deflection response predictions that can be further refined or modified for the application of various other assemblies and structural members.

CHAPTER 6: CONCLUSIONS AND RECOMMENDATIONS

6-1 Conclusion:

The present analytical study is performed on the cyclic behavior of RC frame assemblies strengthened with CFRP sheets and fiber anchorage. The behavior of the strengthened frame members with code-compliant joint was based on the experimental investigation of test data of four frame specimens with different CFRP strengthening schemes in an aim to propose a novel analytical model that predicts the moment-curvature and load deflection response of such assemblies. This work resulted in the following outcomes and conclusions:

- A phenomenological hysteretic load-deflection model is postulated in this work using observations of the experimental hysteresis loops for two frame assemblies to calibrate the key parameters controlling the model layout.
- Excellent agreement was observed between the load-deflection envelope curves developed for these frame assemblies and the experimental envelope curves.
- A simple and effective analysis steps to model hysteresis loop for load-deflection response are presented using phenomenological model.
- The hysteresis loops derived from the presented hysteresis model were in good agreement with the experimental hysteresis loops for the two calibrated specimens and two verification specimens.
- A fully analytical model is presented in this work for any hysteresis cycle that is beyond cracking and up to yielding for the moment-curvature and load-deflection response.
- Material models is developed for concrete under cyclic compression load and cyclic tension load to obtain the stress-strain behavior at different levels within a cycle.

- Excellent agreement was observed for the hysteresis loops predicted by the analytical modeled against the experimental data.
- The verification was applied on multiple specimens two of which are presented in this work.

6-2 Recommendations:

- The presented models reflect an encouraging first step towards a fully analytical model that can be further developed to include cycles beyond yielding and up to ultimate failure.
- More experimental studies for strengthened members of frame assemblies are needed to attain the goal in point 1.
- Investigating the applicability of this model on other strengthened members of assemblies.
- Further refinement of the current presented model is encouraged to include more key points on the hysteresis loop that closely mimic the experimental behavior.

REFERENCES

Abouelleil, A., Rasheed, H.A.(2021). *Calibrating a New Constitutive Tension Model to Extract a Simplified Nonlinear Sectional Analysis of Reinforced Concrete Beams*. Appl. Sci. 2021, 11, 2292. https://doi.org/ 10.3390/app11052292

Al Salloum, Y., Almusallam, T. (2007). *Seismic Response of Interior RC Beam-Column Joints Upgraded with FRP Sheets. I: Experimental Study*. Journal of Composites for Construction.

Al-Salloum, Y. A., N. A. Siddiqui, H. M. Elsanadedy, A. A. Abadel, and M. A. Aqel. (2011). *Textile-reinforced mortar versus FRP as strengthening material for seismically deficient RC beam-column joints*. J. Compos. Constr. 15 (6): 920–933. https://ascelibrary.org/doi/full/10.1061/%28ASCE%29CC.1943-5614.0000222

Bousselham, A. (2010). *State of research on seismic retrofit of RC beam-column joints with externally bonded FRP*. J. Compos. Constr. 14 (1): 49–61. https://doi.org/10.1061/(ASCE)CC.1943-5614.0000049.

Charkas, H., Rasheed, H.A., Melhem, H. (2003). *Rigorous Procedure for Calculating Deflections of Fiber-Reinforced Polymer-Strengthened Reinforced Concrete Beams*. ACI Structural Journal. V.100, No 4. doi: 10.14359/12662

Dowell, O. K., Seible, F., & Wilson, E. L. (1998). *Pivot hysteresis model for reinforced concrete members.* ACI Structural Journal, V.95, No 5. pp. 607-617. doi: 10.14359/575

Elsisi, A.A., Hassan, H., Aboul Nour, L., Sobhy, A. (2021). *Numerical Analysis of FRP Reinforced Frames Under Cyclic Loading*. The Egyptian International Journal of Engineering Sciences and Technology. Vol. 34 (2021) 28–37.

https://www.researchgate.net/publication/350805082_NUMERICAL_ANALYSIS_OF_FRP_REINFORCED_FRAMES_UNDER_CYCLIC_LOADING

Ji, G., G. Li, and W. Alaywan. (2013). *A new fire resistant FRP for externally bonded concrete repair*. Constr. Build. Mater. 42: 87–96. https://www.sciencedirect.com/science/article/pii/S0950061813000718

Lee, J., Kim, J., Oh, G. (2009). *Strength deterioration of reinforced concrete beam–column joints subjected to cyclic loading*. Engineering Structures 31 (2009) 2070–2085. https://www.sciencedirect.com/science/article/pii/S0141029609001163

Ling, Y. C., Mogili, S., & Hwang, S. J. (2022). Parameter optimization for Pivot hysteresis model for reinforced concrete columns with different failure modes. Earthquake Engineering & Structural Dynamics, 51(10), 2167-2187.

Lowes, L.N., Altoontash, A. (2003). *Modeling Reinforced-Concrete Beam-Column Joints Subjected to Cyclic Loading*. Journal of Structural Engineering. https://ascelibrary.org/doi/10.1061/%28ASCE%2907339445%282003%29129%3A12%281686%29

Mansour, M. Hsu, T. (2005). *Behavior of Reinforced Concrete Elements under Cyclic Shear. II: Theoretical Model*. Journal of Structural Engineering. https://ascelibrary.org/doi/full/10.1061/%28ASCE%290733-9445%282005%29131%3A1%2854%29

Mukherjee, A., Joshi.M. (2005). *FRPC Reinforced Concrete Beam-Column Joints Under Cyclic Excitation*. Elsevier. Composite Structures 70 (2005) 185–199

Nayal, R. Rasheed, H.A.(2006). Tension Stiffening Model for Concrete Beams Reinforced with Steel and FRP Bars. Journal of Materials in Civil Engineering, V. 18, No. 6, pp. 743-875. doi: doi:10.1061/ASCE0899-1561200618:6831

Parvin, A., and Wu, S. (2008). *Ply Angle Effect on Fiber Composite Wrapped Reinforced Concrete Beam–Column Connections under Combined Axial and Cyclic Loads*. Composite Structures, V. 82, No. 4, pp. 532-538. doi: 10.1016/j.compstruct.2007.02.004

Pohoryles, D.A., Melo, J., Rossetto, T. Varum, H. Bisby, L. (2019). *Seismic Retrofit Schemes with FRP for Deficient RC Beam-Column Joints: State-of-the-Art Review*. Journal of Composites for Construction. Vol 23, Issue 4. https://ascelibrary.org/doi/epdf/10.1061/%28ASCE%29CC.1943-5614.0000950

Rasheed, H.A., Larson, K. H., & Amiri, S.N.(2013). Analytical Solution of Interface Shear Stresses in Externally Bonded FRP-Strengthened Concrete Beams. Journal of Engineering Mechanics, V.139, No.1, pp. 18-28

Realfonzo, R. Napoli, A., Pinilla, J.G.R. (2014). *Cyclic behavior of RC beam-column joints strengthened with FRP systems*. Elsevier. Construction and Building Materials, V. 54, pp. 282-297. doi:10.1016/j.conbuildmat.2013.12.043. https://www.sciencedirect.com/science/article/pii/S0950061813011999

Reinhardt, H.W. (1984). *FRACTURE MECHANICS OF AN ELASTIC SOFTENING MATERIAL LIKE CONCRETE*. HERON, V.29, No 2. Delft University of Technology. https://repository.tudelft.nl/islandora/object/uuid%3A7e908683-e816-4c4f-928f-03103ed2780e

Saqan, E.I., Rasheed, H.A., Alkhradaji, T. (2020). *Seismic Behavior of Carbon Fiber-Reinforced Polymer-Strengthened Reinforced Concrete Members with Various Anchors*. ACI Structural Journal, V.117, No 4. doi: 10.14359/51723517

Sharma, A., Eligehausen, R., & Reddy, G. R. (2013). *Pivot Hysteresis Model Parameters for Reinforced Concrete Columns, Joints, and Structures*. ACI Structural Journal, V.110, No 2. doi: 10.14359/51684402

Sima, J. F., Roca, P., & Molins, C. (2008). *Cyclic constitutive model for concrete*. Engineering Structures, 30 (2008), pp. 695–706. doi: 10.1016/j.engstruct.2007.05.005

Wang, B., Huo, G., Sun, Y., & Zheng, S. (2019). *Hysteretic behavior of steel reinforced concrete columns based on damage analysis*. Applied Sciences, 2019, 9(4), pp.687; https://doi.org/10.3390/app9040687

Wang, D., Zhao, J., Ju, Y., Shen, H., & Li, X. (2022, October). *Behavior of beam-column joints with high performance fiber-reinforced concrete under cyclic loading*. Structures, V. 44, pp. 171-185. Elsevier.

Zhang, P., Ren, Q., & Lei, D. (2018). *Hysteretic model for concrete under cyclic tension and tension-compression reversals*. Engineering Structures, V.163, pp.388-395. https://www.sciencedirect.com/science/article/pii/S0141029617326640?via%3Dihub